Testing of High-Lift Common Research Model at Takeoff Configurations

Mehti Koklu[1], Judith A. Hannon[2], Latunia P. Melton[3], and Marlyn Y. Andino[4]
NASA Langley Research Center, Hampton, VA, 23681, USA

The 10% scale High-Lift Common Research Model (CRM-HL) was tested in the NASA Langley 14- by 22-Foot Subsonic Tunnel (14x22) in support of the NASA Advanced Air Transport Technology (AATT) Project. The main objective of the wind tunnel test was to improve the aerodynamic performance of a representative aircraft model during takeoff operations using localized active flow control (AFC). This approach involves the application of AFC concepts locally to a relatively small region; therefore, it has the potential to cause minimal architectural change to current aircraft configurations. In addition, the power requirements of localized AFC could be supplied with onboard air resources. Recent exploratory studies identified the aileron as a target area for improving lift-to-drag ratio using localized AFC concepts. The idea is to deflect the ailerons beyond their nominal deflection angles and use AFC to reduce flow separation that occurs at larger aileron deflections. Several AFC concepts with different configurations were evaluated with the goal of achieving high-lift performance improvement. The assessment of AFC configurations is reported in a companion paper. The focus of the current paper is to report the data relevant to the CRM-HL takeoff configurations and establish a reference case for localized AFC application. Three takeoff configurations —reference, nominal, and high-lift improved—are documented. These takeoff configurations are obtained by varying aileron deflection. Wind tunnel measurements including surface static pressures and force and moment data are presented. In addition, surface tuft flow visualization, mainly on the aileron, is provided to understand the flow characteristics developed over the aileron during takeoff.

Nomenclature

α	=	corrected angle of attack
α_{max}	=	stall angle of attack
α_u	=	uncorrected angle of attack
c	=	mean aerodynamic chord
C_p	=	pressure coefficient
C_L	=	lift coefficient
C_{Lmax}	=	maximum lift coefficient
C_D	=	drag coefficient
C_M	=	pitching moment coefficient
δ_a	=	aileron deflection angle
η	=	normalized semispan
L/D	=	lift-to-drag ratio
M	=	freestream Mach number
Re_c	=	Reynolds number based on the mean aerodynamic chord
q	=	freestream dynamic pressure
s	=	model span
x, y, z	=	model coordinates

[1] Research Scientist, Flow Physics and Control Branch, MS 170
[2] Research Scientist, Flow Physics and Control Branch, MS 170
[3] Senior Research Scientist, Flow Physics and Control Branch, MS 170, AIAA Associate Fellow
[4] Research Scientist, Flow Physics and Control Branch, MS 170, AIAA Senior Member

I. Introduction

High-lift systems are critical components of modern transport airplanes, essential for achieving the necessary lift performance during takeoff and landing operations. They are mainly composed of wing leading edge (i.e., slats) and trailing edge (i.e., flaps) devices and allow airplanes to safely take off or land on runways of acceptable length during high-lift operations [1]. Within the framework of efficiency and environmental sustainability goals, it is NASA's mission to improve the high-lift performance of commercial transport airplanes [2-5]. To support these goals, the 10%-scale high-lift version of the Common Research Model (CRM-HL) was built in 2018 under the NASA Advanced Air Transport Technology (AATT) Project. The design and geometry of the CRM-HL model was reported by Lacy and Sclafani [6]. The CRM-HL model is open source and representative of a modern commercial transport airplane. Different configurations based on this geometry establish a broader CRM-HL "ecosystem," which provides a comprehensive set of data for high-lift research, computational fluid dynamics (CFD) code verification, and tunnel-to-tunnel comparisons [7].

The CRM-HL model has been the subject of many tests. An AFC-enabled simplified high-lift version of the model (CRM-SHL-AFC) and the conventional CRM-HL model in landing configuration were tested in the NASA Langley 14- by 22-Foot Subsonic Tunnel (14x22) in 2018 [8-9]. The CRM-HL model was tested again in 14x22 with the open wall configuration to characterize the aeroacoustic performance [10]. The same model was also tested in the QinetiQ (QQ) 5-meter Wind Tunnel in 2019 [11-12]. The QQ test was intended to explore and define the reference high-lift configurations. The test provided force and moment data, surface static pressure data, and surface flow visualization with tufts and oil flow on both the landing and takeoff configurations at different Reynolds numbers. In addition, the QQ test also explored the optimal positioning (gap, overhang, chine location, etc.) of the high-lift devices (slat and flap) [11-12]. Different versions of the CRM-HL model, such as the NASA 5.2% scale semispan model and NASA 2.7% scale full-span model, have been built and tested for exploring Reynolds number and tunnel installation effects within the CRM-HL ecosystem [13-14].

The CRM-HL model has been used to study different AFC approaches to improve high-lift performance. The initial test with the CRM-SHL-AFC configuration focused on the feasibility of replacing Fowler flaps with simple-hinged flaps while maintaining the required high-lift performance with the help of AFC systems [8, 15]. Wind tunnel test results proved that the AFC-enabled simple-hinged flaps could provide high-lift performance superior to the reference conventional CRM-HL model with Fowler flaps. Although the test campaign was successful, the architectural modifications required to replace the Fowler flaps with simple-hinged flaps and supply pneumatic power to the AFC systems were found to be significant. Therefore, a configuration like the CRM-SHL-AFC is perceived as a far term technology for improving fuel burn of a commercial transport airplane [16-18].

As indicated in Ref. [17], a more practical approach could be to use localized AFC, which involves the application of AFC concepts locally to a relatively small region. Therefore, localized AFC could require minimal architectural modification to current aircraft configurations. In addition, power requirements of localized AFC could be supplied with onboard air resources. Localized AFC was motivated by system tradeoff studies that showed even a small percentage improvement in high-lift performance may provide substantial environmental and economic benefits. For example, according to Ref. [19], a 1% increase in takeoff *L/D* is equivalent to a 2,800 lb. increase in payload or a 150 nm increase in range. Recent exploratory studies by Boeing identified several potential applications of localized AFC including the aileron, slat cove, and nacelle pylon region [20]. Localized AFC to improve aileron aerodynamics appears to be the most promising application, as the previous CFD studies indicated meaningful *L/D* improvement during takeoff operations [17, 20].

Ailerons are flight control surfaces that are usually located on the outboard section of the wing. They act as plain trailing-edge flaps and are used to control airplane stability. The ailerons are symmetrically placed on the outer wing but usually operate 180° out of phase. They change lift generation locally to control the rolling moment. Improving the aerodynamics of ailerons involves deflecting the ailerons more than the nominal deflection angles to generate additional lift during takeoff. However, as shown in previous studies, deflecting the ailerons more than nominal results in flow separation that limits or sometimes negates the aerodynamic improvement. Therefore, localized AFC on an aileron involves deflecting an aileron more than the nominal deflection angle and utilizing AFC to control flow separation at increased aileron deflection angles.

The effect of localized AFC on an aileron was investigated numerically in Ref. [17] for a representative future short/medium-range twin-engine airplane. Several AFC configurations were used to investigate the aerodynamic enhancement as well as AFC pneumatic power requirement. CFD results indicated more than a 5% improvement in *L/D* performance during takeoff when attached flow is maintained on the aileron. In addition, the results also showed that localized AFC on an aileron improves C_L and C_{Lmax}, which are important parameters for both takeoff and landing

operations. It should be noted that all these improvements are within the capability of onboard fluidic sources such as an auxiliary power unit (APU).

The potential net performance benefits of localized AFC application on an aileron are studied in Ref. [21] using the numerically predicted aerodynamic performance improvement. The system integration study indicated a net performance improvement even when considering the AFC systems, power sources, and structural integration weight penalties. For example, a 2 – 5% potential net gain in aircraft *L/D* is estimated using localized AFC on ailerons during takeoff, including assessed trim and aeroelastic/structural impacts. This net improvement could translate into a 0.5% block fuel/seat performance improvement, which would provide a substantial environmental and economic impact [21].

Motivated by the successful CFD and system integration studies, a wind tunnel test campaign was completed to determine the performance improvement of localized AFC on the 10% scale CRM-HL model [18]. The *L/D* performance of the CRM-HL model at previously defined takeoff configurations was measured. Several AFC concepts with different configurations were evaluated with the goal of achieving improved high-lift performance. The assessment of the AFC configurations will be reported in a companion paper [22].

The focus of the current paper is to report the data relevant to the CRM-HL takeoff configurations. Three different takeoff configurations—reference, nominal, and high-lift improved—are obtained by varying aileron deflection. Another objective of this paper is to establish a reference case for the current localized AFC application as well as any future flow control applications during takeoff. The paper presents the wind tunnel measurements including static surface pressures and force and moment data. In addition, surface tuft flow visualizations, mainly on the aileron, will be provided to understand the flow characteristics that developed over the aileron of the CRM-HL model at different takeoff configurations.

II. Experimental Setup

The wind tunnel test was performed in 14x22, which is an atmospheric, closed return wind tunnel with a 9:1 contraction ratio [23]. The test section was configured with closed walls, which provided a 14.5-ft high, 21.75-ft wide, and 50-ft long test section. The majority of the test was performed at a nominal freestream Mach number of 0.2 and a corresponding dynamic pressure of 60 psf. The Reynolds number based on the mean aerodynamic chord (27.6 in. at y = 46.9 in.) is approximately $3x10^6$. The turbulence intensity in the tunnel varies with dynamic pressure (q) and location and was reported as 0.07% - 0.08% for q = 60 psf [24]. Wind tunnel data can be corrected using classical correction methods, the Heyson method, and the Transonic Wall Interference Correction System (TWICS) [25]. We will report the TWICS corrected data in this study.

A. Wind Tunnel Model

The model tested in this study is the 10%-scale high-lift version of the NASA Common Research Model. A photo of the CRM-HL in the 14x22 is shown in Fig. 1. The details of the CRM-HL model can be found in Refs. [6-12]. The 9.64 ft. high semispan model was installed vertically on the turn table in the tunnel floor. The length of the fuselage is 20.59 ft. The CRM-HL model was designed and fabricated to be modular, which enabled the model to be switched between different configurations while keeping the other components unchanged. The tested CRM-HL model includes a fuselage, wing, leading edge slat, trailing edge flaps, and a flow through nacelle. The model also includes a wing/fuselage strake and a nacelle chine to represent a typical transport airplane (Fig. 1). The model was installed on top of a 3.5-in. peniche that was attached to the turntable, whereas the fuselage/model is connected to the force balance below the model. A labyrinth seal provided the interface between the fuselage and the peniche. The nacelle has the original inlet lip and does not have the modifications referred to in Ref. [11]. Transition dots with a height of 0.01 in. and a diameter of 0.05 in. were installed at the locations illustrated in Fig. 1 on the wing upper surface.

For the takeoff configurations, both the inboard and outboard flap deflections were 25°, as defined by Refs. [6, 11-12]. The inboard flap was connected to the main element using one internal and one external bracket. The outboard flaps were supported by two external brackets. These brackets were covered by flap fairings, which also contained the pressure tubing. On the other hand, the leading-edge slat was deflected to 22°. The slats were attached to the main element by 15 slat brackets. The slat bracket design included channels for routing the pressure tubing to the main element. The takeoff configuration was defined as the sealed slat configuration [11-12], and accordingly, the slat gap between the slat and main element was sealed on the underside (i.e., slat cove). An example of the sealed slat and slat bracket is shown in Fig 2. A new outboard wing section with an aileron, which was defined by Boeing [26], was built to enable different takeoff configurations [18]. The aileron was attached to the outboard wing using fixed brackets that enabled the aileron deflection angles of 0°, 7.5°, 16°, and 25°. Sample sectional wing profiles are presented in Fig. 3 for inboard, midboard, and outboard wing, both with and without aileron deflections.

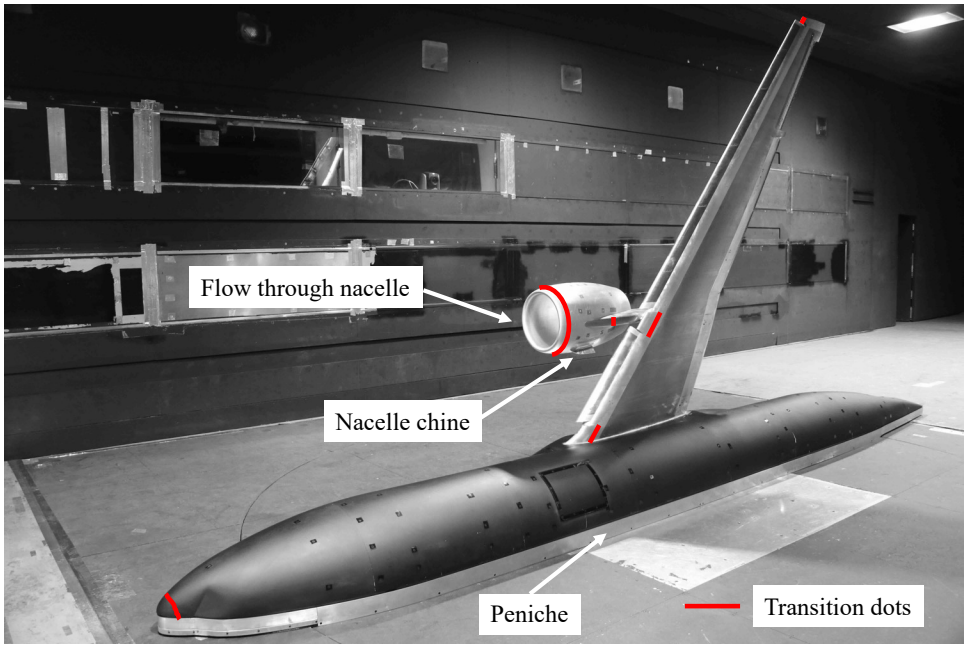

Fig. 1 CRM-HL model in the 14x22 tunnel [Source NASA].

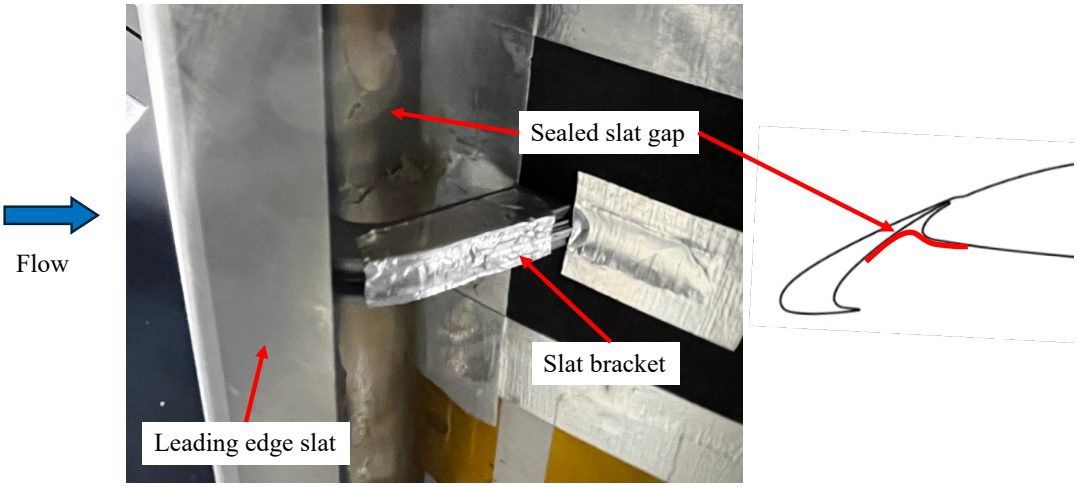

Fig. 2 Sample view of the leading-edge slat showing underside. The slat gap is sealed using tape as shown in the 2D cut [Source NASA].

Fig. 3 Sectional wing profiles of the CRM-HL model in takeoff configuration: (a) inboard, (b) midboard, (c) outboard, and (d) outboard with deflected aileron. Vertical dashed line shows the aileron hinge line.

The pressure orifice layout of the 10% scale CRM-HL model is presented in Fig. 4. The original model had more than 720 pressure orifices mostly populated along streamwise rows at eight spanwise locations. These locations are commonly shown in nondimensional form η = y/s x 100, where s = 115.7 in. Compared to the original outboard section, there are fewer pressure orifices, especially at the η = 82% (y = 95 in.) and η = 91% (y = 105 in.) locations due to the additional AFC hardware. In addition to these locations, we will provide streamwise pressure distributions from the pressure orifices at η = 24% (y = 28 in.) and η = 55% (y = 64 in.) as representative of inboard and midboard wing performance.

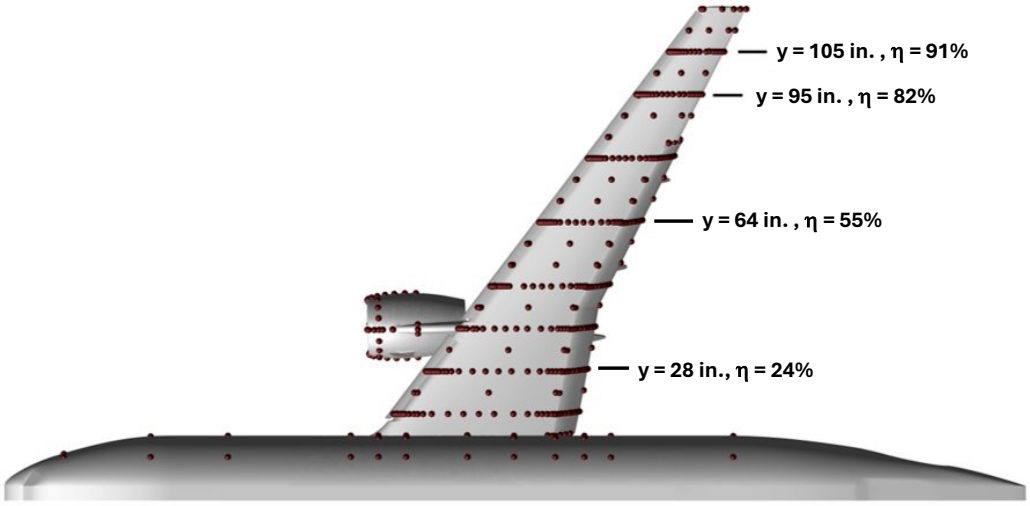

Fig. 4 Surface pressure orifices on the CRM-HL model.

B. Measurement Data

As mentioned before, the data presented in this paper were corrected for wind tunnel wall interference using the Transonic Wall Interference Correction System (TWICS) method [25]. The effect of applying wall correction is seen in Fig. 5a. The application of TWICS typically increased the angle of attack by ~0.4° near α = 0° and ~0.9° at higher angles of attack. It also decreases the lift coefficient and increases the drag coefficient as much as ~0.03.

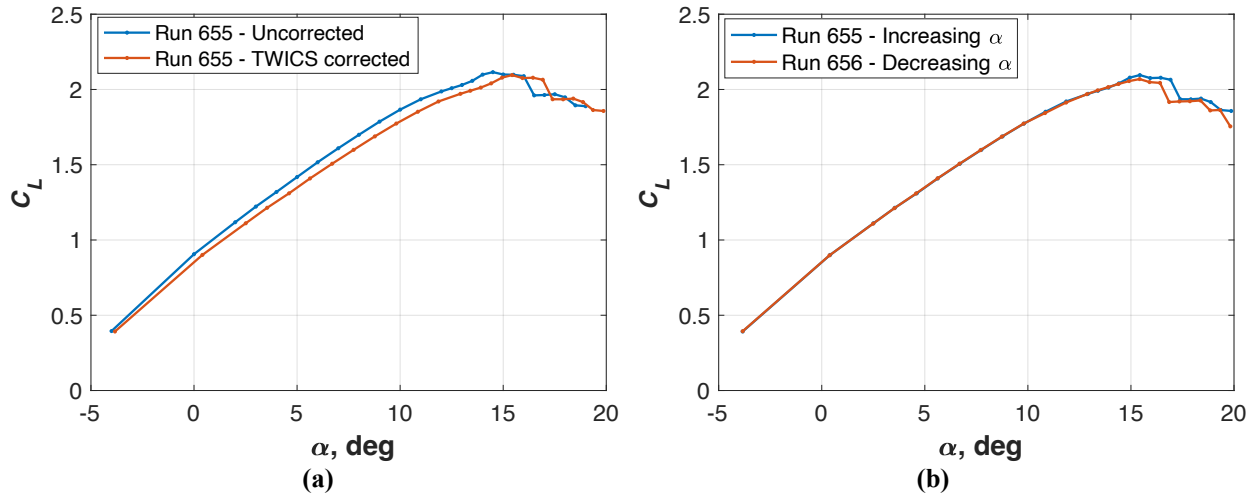

Fig. 5 C_L - α plots showing the effect of (a) wind tunnel correction and (b) hysteresis (M = 0.2, Re_c = 3.0x10^6).

The hysteresis effect associated with increasing and decreasing angle of attack is shown in Fig. 5b (Runs 655 and 656, respectively). The results indicate little or no hysteresis due to increasing and/or decreasing angle of attack until stall. After C_{Lmax}, increasing α produced slightly higher C_L values than the decreasing-α case. This is possibly due to flow separation over the nacelle. Flow stays attached for larger angles of attack for increasing α; however, once flow is separated, reducing the angle of attack does not reattach flow. Pressure distribution over the nacelle (not shown

here) also indicates attached vs. separated flow for increasing and decreasing α near C_{Lmax}. Relatively smaller hysteresis effect was shown on the landing configuration [9]; however, the configuration difference, especially the sealed slat gap in the takeoff configuration, possibly increased the hysteresis effect.

Before we present the wind tunnel data, we will provide a sample of the data repeatability information for a takeoff configuration. These repeatability results help us to understand the confidence levels (±2σ - 95%) in the data being presented. Because of relatively small differences between the three takeoff configurations, we will only provide repeatability information for the takeoff configuration with aileron deflected to 16° (δ_a = 16°) as it has more repeat runs. There were a total of 14 repeat runs for this particular case, where almost half of them cover the full angle of attack range and the other half cover the potential takeoff angle of attack ($0° \le \alpha \le 11°$) range. Fig. 6 shows the variation of the residuals for the lift coefficient (C_L), drag coefficient (C_D), pitching moment coefficient (C_M), and L/D with angle of attack. Residuals were calculated with respect to the corresponding average values of the repeat runs at each angle of attack. Then, the standard deviation was calculated for each angle of attack. The two times the standard deviation (±2σ values) are shown as black dashed line. The figure also shows the expected instrumentation uncertainty (shown as blue dashed line), which was calculated using propagation of errors through the data reduction equations, again, based on 95% confidence levels.

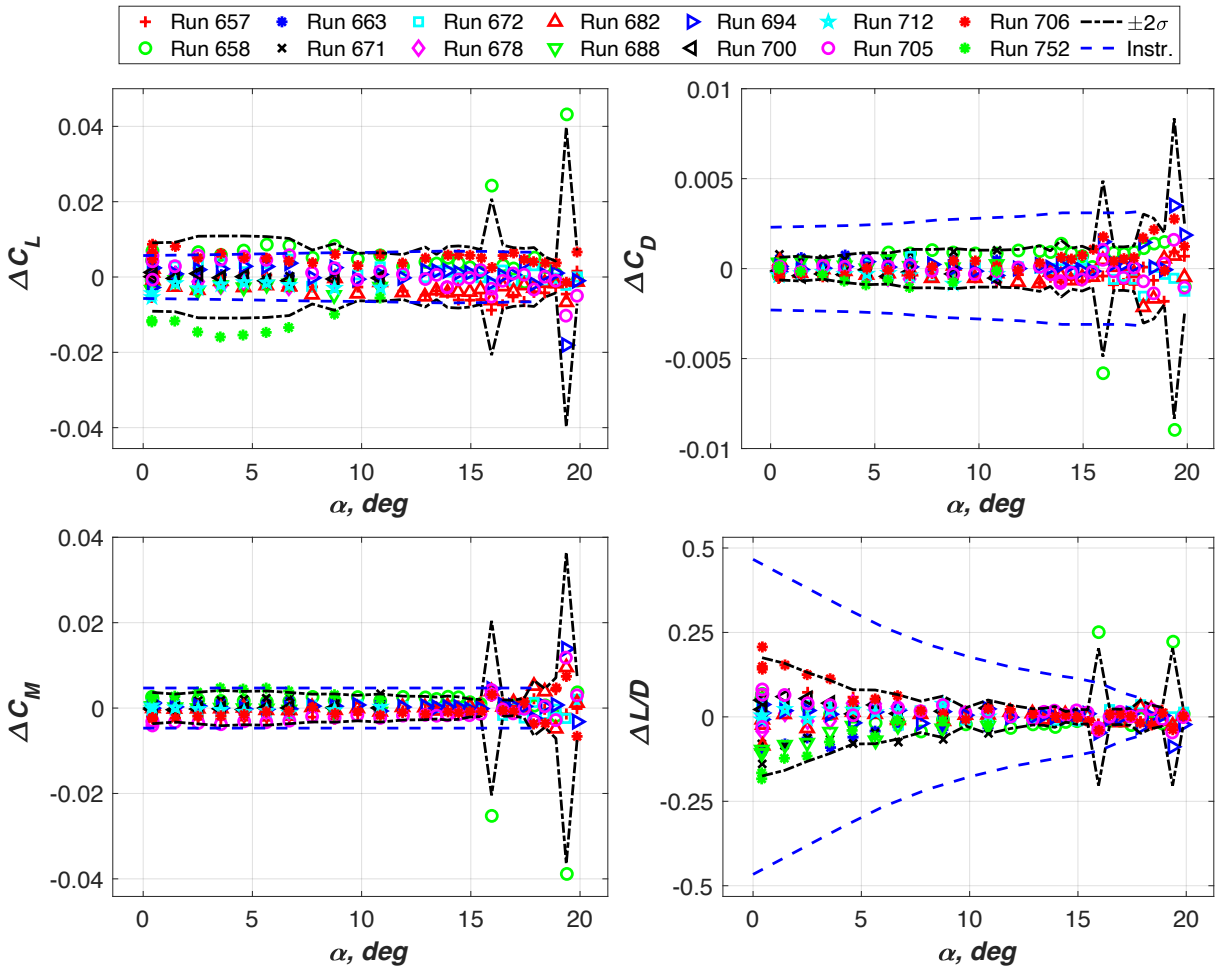

Fig. 6 Calculated residuals from the mean for the lift coefficient, drag coefficient, pitching moment coefficient, and lift-to-drag ratio (M = 0.2, q = 60 psf, δ_a = 16°).

These plots indicate that the variations in C_D, C_M, L/D coefficients are well within the measurement uncertainty for most angles of attack, except near stall. Near stall, Run 658 produced a few outlier points and resulted in a prediction interval that is larger than the instrumentation uncertainty. Run 752 produced outlier points in ΔC_L at lower angles of attack, which resulted in a prediction interval slightly larger than the instrumentation uncertainty. Note that Run 752 is the last run at the end of the test.

III. Results

The main focus of this study is to present data related to the takeoff configurations of the CRM-HL model. These different takeoff configurations are obtained by varying the aileron deflection angle (δ_a) while keeping other settings the same. The new outboard wing section of the CRM-HL was designed to include an aileron with fixed brackets for aileron deflection angles of 0°, 7.5°, 16°, and 25° [18]. The nondeflected aileron ($\delta_a = 0°$) is referred to as the reference takeoff configuration that was defined in Refs. [11-12] and is the takeoff configuration of the CRM-HL ecosystem. In this configuration, the outboard section of the wing is composed of a slat and main element combination (i.e., without flap) as shown in the Fig. 3c. However, during takeoff, airplanes usually benefit by deflecting the aileron slightly to increase the wing camber and hence take advantage of increased C_L and L/D. In the second takeoff configuration, the aileron is deflected to 7.5°, which will be referred to as the nominal takeoff configuration. Continuing the same principle of improving the takeoff performance by aileron deflection, our third takeoff configuration comprises even more aileron deflection ($\delta_a = 16°$ and $\delta_a = 25°$). This takeoff configuration is intended to be used together with a flow control strategy as the larger aileron deflection causes flow separation over the aileron. This flow separation is detrimental to the takeoff performance, which increases the drag and hence lowers L/D. The results of the flow separation control over the aileron surface will be reported in a companion paper [22]. The current paper presents the wing tunnel test results without flow control.

A. Reference Takeoff Configuration, $\delta_a = 0°$

The takeoff configuration with nondeflected aileron was briefly tested in the QinnetiQ (QQ) 5m wind tunnel using the same 10% CRM-HL model [11-12]. The most noticeable difference from the landing configuration, in addition to the 25° slat and 22° flap deflections, is the sealed gap between the slat and main element. The sealed slat case is chosen to provide a simpler flow field without slat bracket wake effects for CFD modeling [11].

The takeoff lift curve obtained in this test compares well with the previous QinetiQ test results (Fig. 7a). Note that the QQ results compared in this figure is with the original nacelle cowl but without floor blowing system. It was shown that these two modifications greatly affect the lift curve near the C_{Lmax} region. We see a good agreement until C_{Lmax}. The post stall lift curve experiences a sudden drop in lift, which was attributed to nacelle cowl flow separation [11]. Overall trend in the drag coefficient is similar (Fig. 7b); however, the current test produced slightly higher ($\Delta C_D \sim 0.005$) drag values compared to the QQ tests. Within the framework of CRM-HL ecosystem, the CRM-HL takeoff configuration was also tested using the semispan 5.2% CRM-HL model and results are reported in Ref. [27]. Although the 5.2% scale results indicated lower C_{Lmax} ($C_{Lmax} = 1.95$ vs. $C_{Lmax} = 2.1$) compared to the current and QinetiQ test results, note that the 5.2% CRM-HL model has slight modifications from the original 10% CRM-HL geometry, such as re-designed nacelle, trailing edges, and flap fairings.

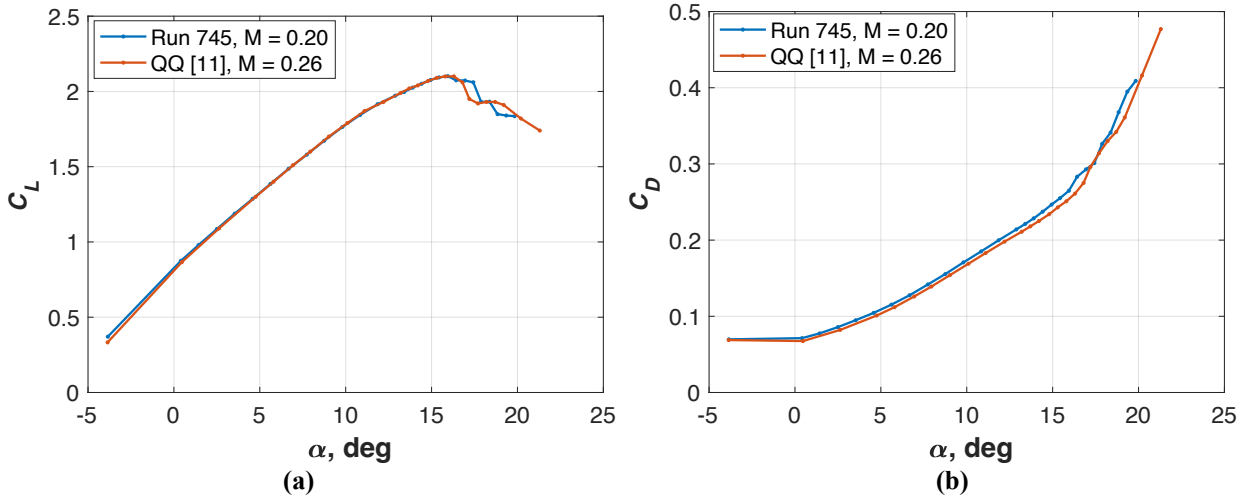

Fig. 7 Comparison of the current results to the QinetiQ results [11] (a) lift coefficient and (b) drag coefficient.

First, the effect of Reynolds number on the wind tunnel measurements is presented (Fig. 8). The initial idea was to test the model at Mach number of 0.26, which is the defined takeoff Mach number. However, due to the labyrinth seal fouling issues for $\alpha_u > 8°$, the reference takeoff Mach number was reduced to 0.2. The maximum Mach number was also reduced to 0.23 in the 5.2% scale model test at the Low-Speed Wind Tunnel at Braunschweig [27]. Although

we did not use 0.26 as the reference Mach number, we tested the configuration from Mach number 0.1 to 0.26 to see the effect of Reynolds number. The corresponding Reynolds numbers based on the mean aerodynamic chord, Re_c, are 3.9×10^6, 3.0×10^6, 2.2×10^6, and 1.5×10^6 for $M = 0.26$, $M = 0.20$, $M = 0.15$, and $M = 0.10$, respectively.

Here we are presenting the effect of Reynolds number on the aerodynamic characteristics. Note that the $M = 0.26$ case only covers the linear region of the lift curve where we had to stop before reaching C_{Lmax}. As shown in the inset figure, we see a small but consistent shift ($\Delta C_L \sim 0.05$) in the linear region of the lift curve as the Reynolds number increases (Fig. 8a). There is a significant jump ($\Delta C_L \sim 0.1$) from $M = 0.1$ to $M = 0.15$ near stall whereas data from the other Mach numbers are very close. C_{Lmax} values are 1.98, 2.06 and 2.1, and corresponding α_{max} are 15.9°, 16.9°, and 15.9° for $M = 0.1$, $M = 0.15$, and $M = 0.2$, respectively. These C_{Lmax} values are slightly higher than those of the 5.2% CRM-HL test results [27]. The drag coefficient values are very close for $\alpha < 13°$ (Fig. 8b); however, we see some difference near or after stall, similar to the lift curve. The pitching moment (C_M) is negative for all prestall angles of attack (Fig. 8c) indicating nose-down pitching moment as expected from a typical high-lift wing [3]. The C_M slightly offsets as the Mach number increases, which is consistent with the slight increase in lift at lower angles of attack. We observe greater variations in C_M at higher angles of attack. Similarly, the $M = 0.1$ case produced the lowest L/D for the entire α range (Fig. 8d). Although we see a gradually higher L/D peak near $\alpha = 2°$, the $M = 0.15$ and $M = 0.2$ cases agree well for the rest of the regions. With the limited data, it appears that the $M = 0.26$ case agrees with the $M = 0.2$ case.

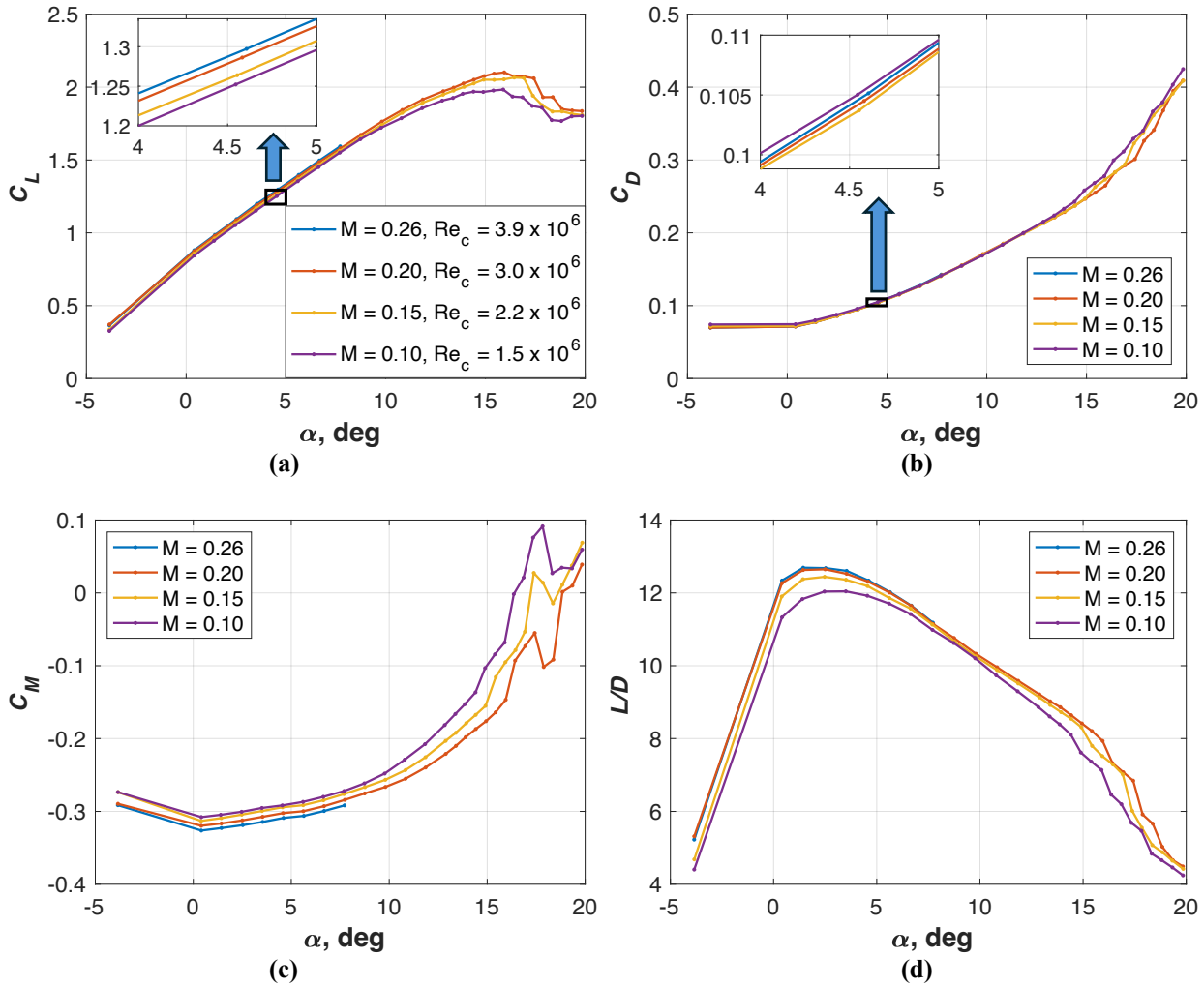

Fig. 8 The effect of Reynolds number on the aerodynamic parameters for the reference takeoff configuration ($\delta_a = 0°$). (a) lift coefficient, (b) drag coefficient, (c) pitching moment coefficient, and (d) lift-to-drag ratio.

The sectional pressure distributions give more detail on the differences observed in the force measurements. Fig. 9 shows the C_p distribution at C_{Lmax} ($\alpha = 15.9°$) over the inboard section ($\eta = 24\%$). The C_p distributions are broken into subplots where the pressures on the slat, the main element, and the flap are given in the left, middle, and right plots, respectively. The $M = 0.1$ case produced slightly lower suction pressures over the inboard wing whereas the $M = 0.15$ and $M = 0.2$ cases produce similar C_p distributions. The main difference is over the inboard flap, where the C_p distributions indicate separated flow for $M = 0.1$ but attached flow for $M = 0.15$ and $M = 0.2$. As a result, the separated flow over the inboard flap explains the lower lift generation for $M = 0.1$. For the midboard wing (Fig. 10), again the $M = 0.1$ case produces slightly lower suction pressures whereas the $M = 0.15$ and $M = 0.2$ cases are close to each other. Although the trailing edge C_p distribution indicates separated flow for all three Mach numbers, the $M = 0.1$ results indicate a slightly larger separation bubble and correspondingly lower suction peaks over the flap.

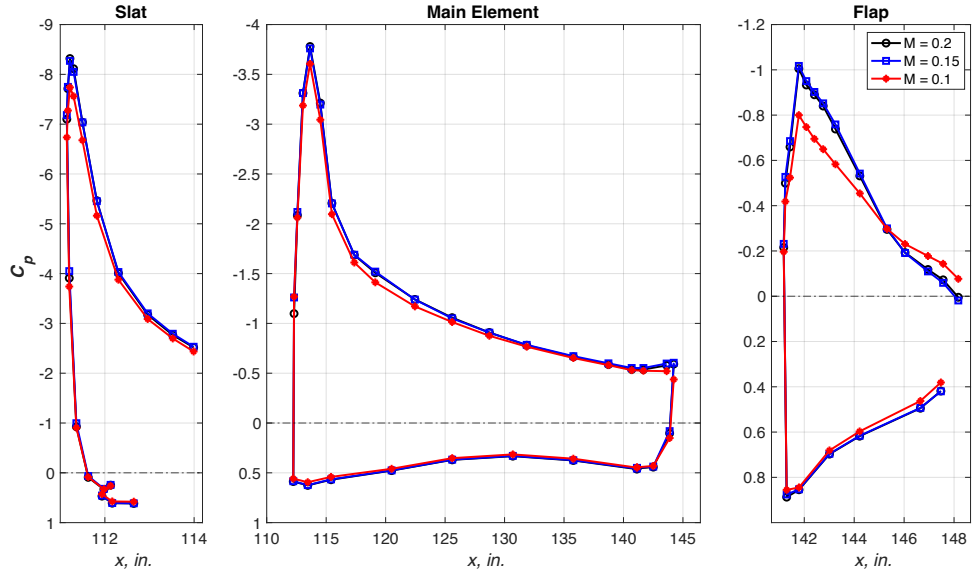

Fig. 9 Streamwise C_p distributions over the inboard section ($\eta = 24\%$, $\delta_a = 0°$, $\alpha = 15.9°$).

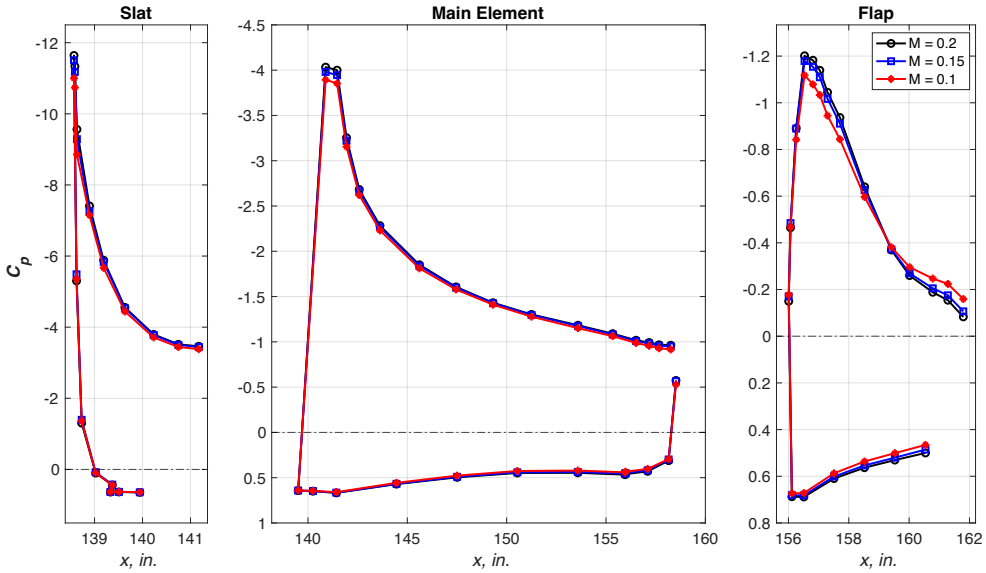

Fig. 10 Streamwise C_p distributions over the midboard section ($\eta = 55\%$, $\delta_a = 0°$, $\alpha = 15.9°$).

The effect of different Mach numbers is more noticeable in the C_p distribution over the outboard sections (Fig. 11). Higher Mach numbers produce higher suction pressures both over the slat and main element (Fig. 11a). The C_p distributions indicate separated flow over the main element for the $M = 0.1$ and $M = 0.15$ cases, whereas the flow is

separated only over the aileron section for $M = 0.2$ at the $\eta = 82\%$ location. For the most outboard location ($\eta = 91\%$), the flow over the main element is separated for all three Mach numbers; however, the flow separated farther downstream for the $M = 0.2$ case (Fig. 11b). These observations are in line with the slightly lower lift values of the $M = 0.1$ and $M = 0.15$ cases compared to the $M = 0.2$ case near C_{Lmax}.

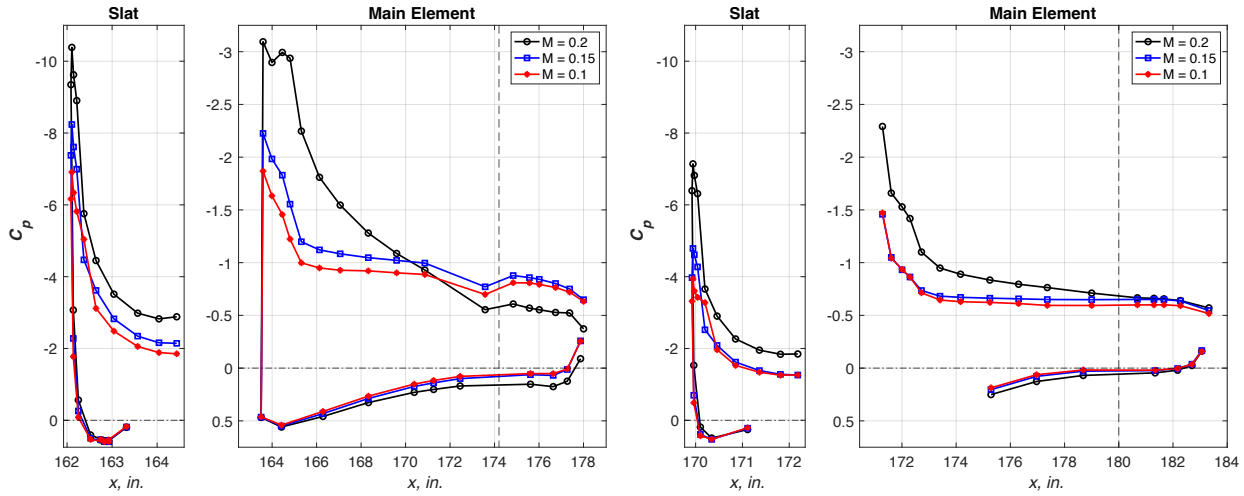

Fig. 11 Streamwise C_p distributions over the outboard sections (a) $\eta = 82\%$ and (b) $\eta = 91\%$. Vertical dashed lines indicate the aileron hinge location ($\delta_a = 0°$, $\alpha = 15.9°$).

Next, we will examine the pressure distributions at various angles of attack for the reference takeoff Mach number ($M = 0.2$). As expected, we have higher suction pressures over the slat and main element as we increase the angle of attack until stall at $\alpha = 15.9°$ (Fig. 12). The higher suction pressures result in higher lift coefficients. For the post-stall angle of attack ($\alpha = 17.9°$), the C_p distribution indicates separated flow over the inboard wing (near $x \sim 120$ in.). Over the inboard flap, the suction pressures decrease with angle of attack. Flow over the inboard flap is attached except for $\alpha = 17.9°$. The separated flow over the inboard flap for $\alpha = 17.9°$ also caused lower suction pressures near the trailing edge of the main element. A similar conclusion can be drawn for the midboard wing where the larger angle of attack produced higher suction pressures on the slat and main element and lower suction pressures on the flap (Fig. 13). Although the pressure distribution indicates clear separated flow near the flap trailing edge for $\alpha = 17.9°$, the flow is either attached or there is a very small trailing edge separation for the prestall angles of attack.

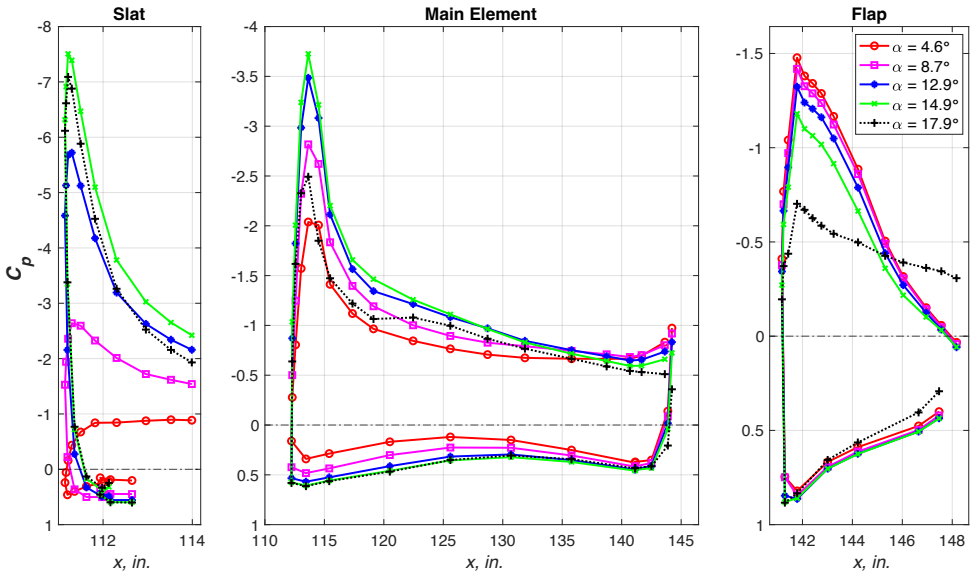

Fig. 12 C_p variation with α over the inboard section ($\eta = 24\%$, $\delta_a = 0°$, $M = 0.2$).

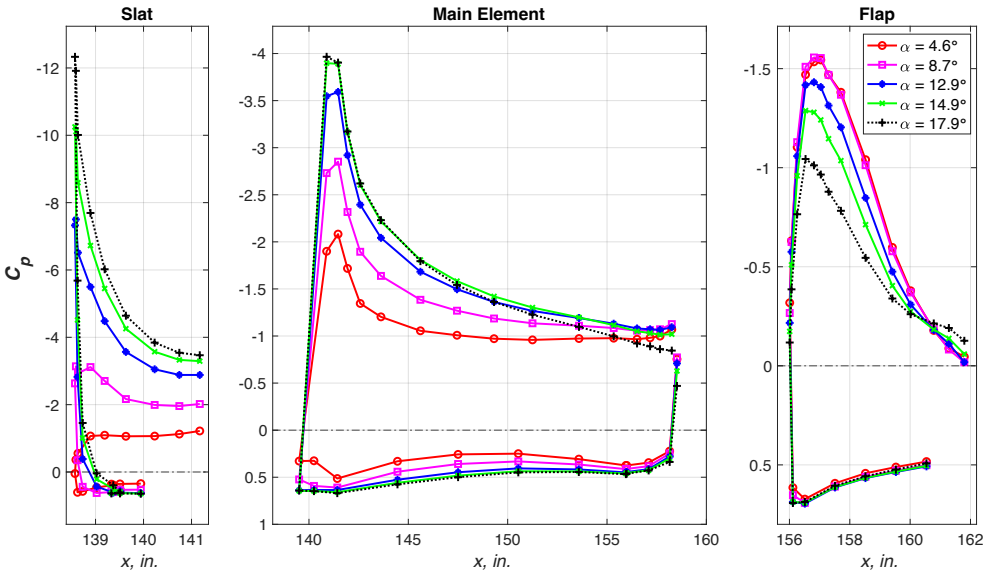

Fig. 13 C_p variation with α over the midboard section ($\eta = 55\%$, $\delta_a = 0°$, $M = 0.2$).

The C_p distributions for the two outboard sections are presented in Fig. 14. In this figure, the vertical dashed lines indicate the aileron hinge location. Note, however, that the aileron is nondeflected ($\delta_a = 0°$) for this case. Increasing the angle of attack results in gradually higher suction pressures both over the slat and main element until stall. There is a kink in the C_p distributions near the leading edge of the main element. Although not for certain, this could be due to a small separation bubble that is possibly generated by a curvature discontinuity (where the slat would be stowed during cruise) and a step (due to overlapped slat trailing edge). For post stall ($\alpha = 17.9°$), the suction pressures are lower on the main element due to flow separation that starts near $x \sim 165$ in. ($\eta = 82\%$, Fig. 14a). This demands a lower pressure recovery over the slat; therefore, we see lower suction pressures near the trailing edge of the slat despite the large suction peak. The flow near the aileron trailing edge appears to be attached for $\alpha = 4.6°$. The C_p distribution indicates a small trailing edge flow separation for $\alpha = 8.7°$, and the separation location moves upstream as α increases. A similar conclusion can be drawn for the most outboard location ($\eta = 91\%$, Fig. 14b). We see higher suction pressures both over the slat and main element until stall. The flow over the aileron is attached for $\alpha = 4.6°$ and separated for higher angles of attack. In addition to the lower suction pressures, the main difference between the two outboard locations is that the flow over the main element separates earlier for the most outboard location (at $\alpha = 14.9°$ vs. $\alpha = 17.9°$). For $\alpha = 17.9°$, flow separation moves farther upstream, reaching near the trailing edge of the slat ($x \sim 173$ in.).

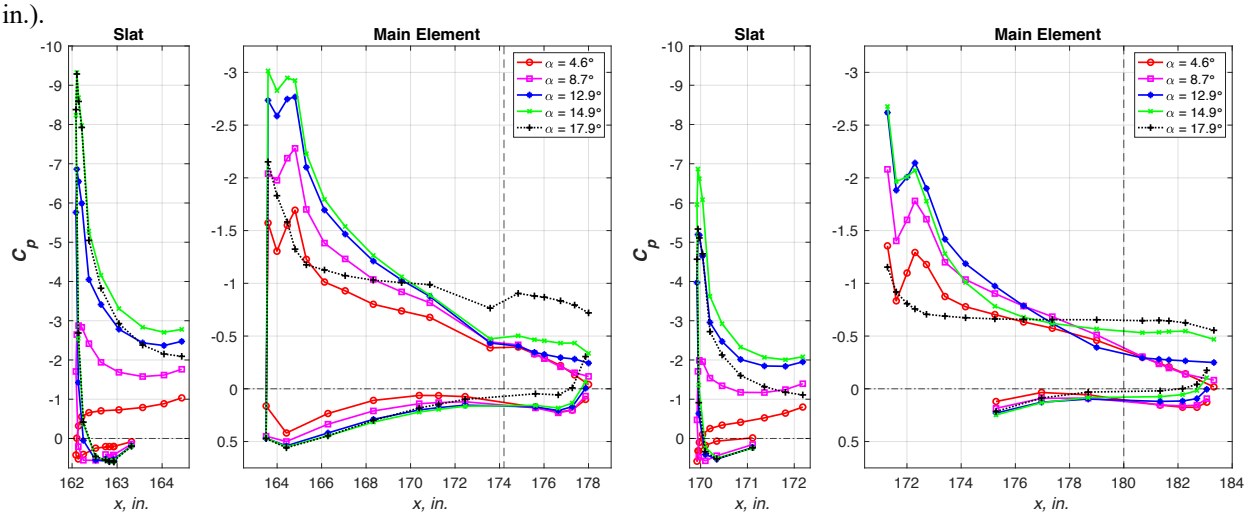

Fig. 14 C_p variation with α at (a) $\eta = 82\%$ and (b) $\eta = 91\%$ sections for the reference takeoff configuration ($\delta_a = 0°$, $M = 0.2$). Vertical dashed lines indicate aileron hinge location.

Figure 15 shows limited tuft flow visualization over the aileron. The inset shows the location of the aileron compared to the entire wing. For the nondeflected aileron, flow appears to be attached at $\alpha = 4.6°$, consistent with the C_p distribution. When the angle of attack increased to 8.7°, most of the flow over the aileron is still attached. The tuft resolution may not be enough to capture the trailing edge flow separation shown in the C_p distribution. Flow separation moves upstream as we increase the angle of attack, and the flow over the entire aileron is separated for $\alpha = 17.9°$, consistent with the C_p distribution.

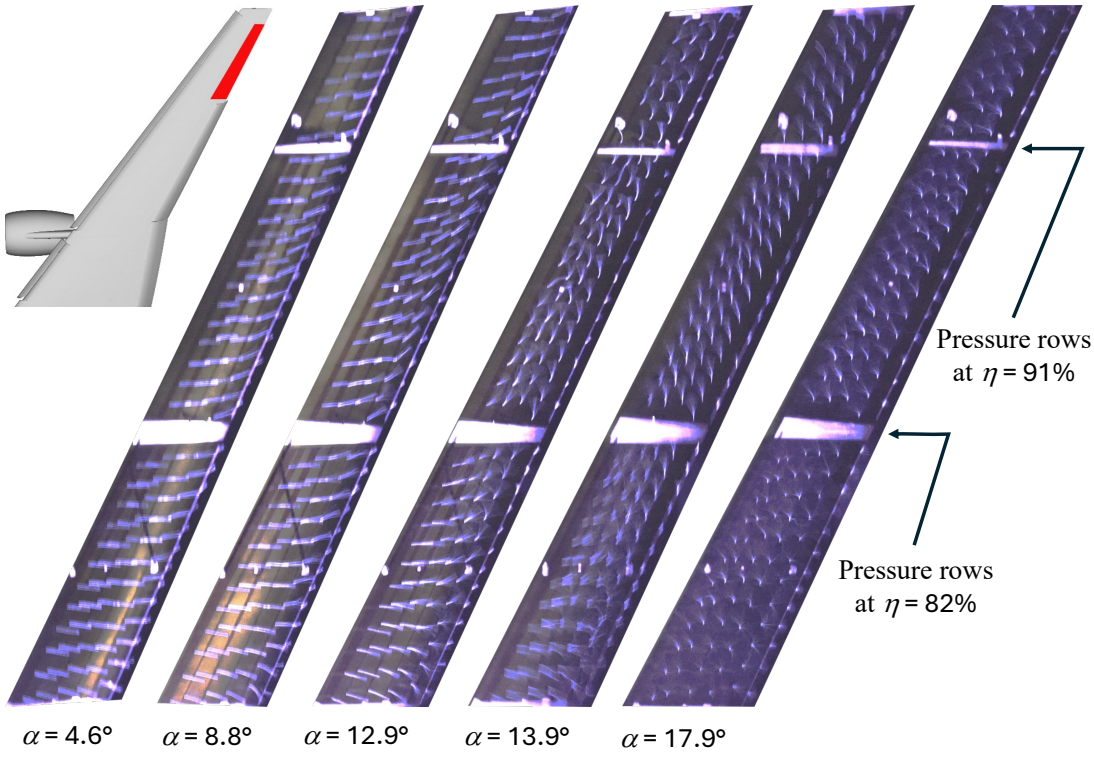

Fig. 15 Tuft flow visualization over the aileron ($\delta_a = 0°$, $M = 0.2$).

B. Nominal Takeoff Configuration, $\delta_a = 7.5°$

For improved aerodynamic performance during takeoff, airplanes usually take advantage of the ailerons which exist for flight stability and control. In this setting, the ailerons are used as trailing edge flaps that are deflected to increase the aerodynamic performance by increasing the local wing camber. Ailerons on each side of the wing are deflected symmetrically to not cause any flight control issues. The aileron deflection angle should be maximized to enhance performance but kept minimal to avoid any flow separation. Even a small flow separation can cause an increase in drag, which will dramatically decrease the L/D and takeoff performance. This optimization problem yields a nominal aileron deflection of 7.5° for the takeoff configuration [20].

Figure 16a shows lift curves for multiple runs at the nominal takeoff configuration ($\delta_a = 7.5°$) together with the lift curve for the nondeflected aileron ($\delta_a = 0°$) case. We see very good repeatability, especially at lower angles of attack ($\alpha < 13°$). For all nominal takeoff configuration cases, α_{max} is 15.4°, which is 0.5° lower than the nondeflected case. However, the lift curve is flatter between $\alpha = 15.5°$ and $\alpha = 17.5°$, and the lift values are very close in this region. As shown in this figure, by deflecting the aileron to $\delta_a = 7.5°$, C_L is improved by 0.03 at lower angles of attack. The lift curve gradually converges to that of the nondeflected case near C_{Lmax}. The aileron deflection of 7.5° also increases the drag for $\alpha > 6°$; however, the difference is small (10 counts) and close to the measurement repeatability (Fig. 16b).

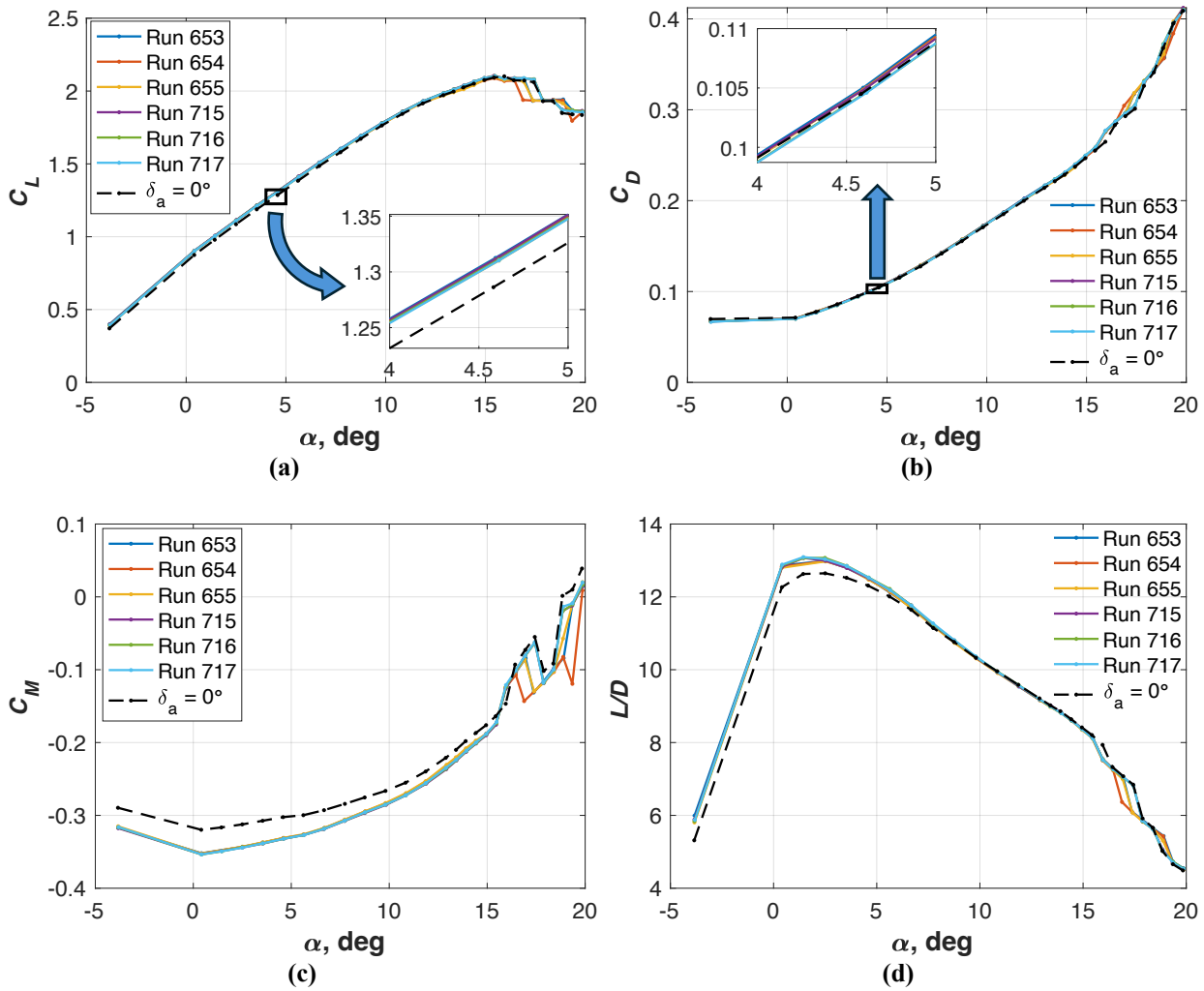

Fig. 16 Aerodynamic parameters for the nominal takeoff configuration (δ_a = 7.5°). (a) lift coefficient, (b) drag coefficient, (c) pitching moment coefficient, and (d) lift-to-drag ratio.

As expected, the aileron deflection and hence the lift increase has a larger impact on the pitching moment coefficient (Fig. 16c). As compared to the nondeflected case, deflecting the aileron generates a more negative (nose down) pitching moment for the entire angle of attack range; however, it is more pronounced at lower (i.e., takeoff) angles of attack. The effect of aileron deflection is also evident in *L/D*, which is an important parameter during takeoff (Fig. 16d). As compared to the nondeflected case, the nominal aileron deflection provides as much as a 0.5 increase in *L/D* at $\alpha = 1.5°$ that gradually converges to the *L/D* values for the nondeflected case near $\alpha = 10°$.

Streamwise C_p distributions over the inboard and outboard wings are presented in Figs. 17-18. Since the only difference between the deflected and nondeflected aileron is only over the outboard wing, the C_p distributions for the inboard and midboard sections are similar to those of the nondeflected case in Figs. 12-13. We have higher suction pressures over the slat and main element as we increase the angle of attack until stall ($\alpha = 15.4°$), whereas the suction pressures decrease with the angle of attack over the flap region. The C_p distribution indicates separated flow over the main element for post stall ($\alpha = 17.9°$). Flow over the inboard and midboard flaps is attached except for $\alpha = 17.9°$.

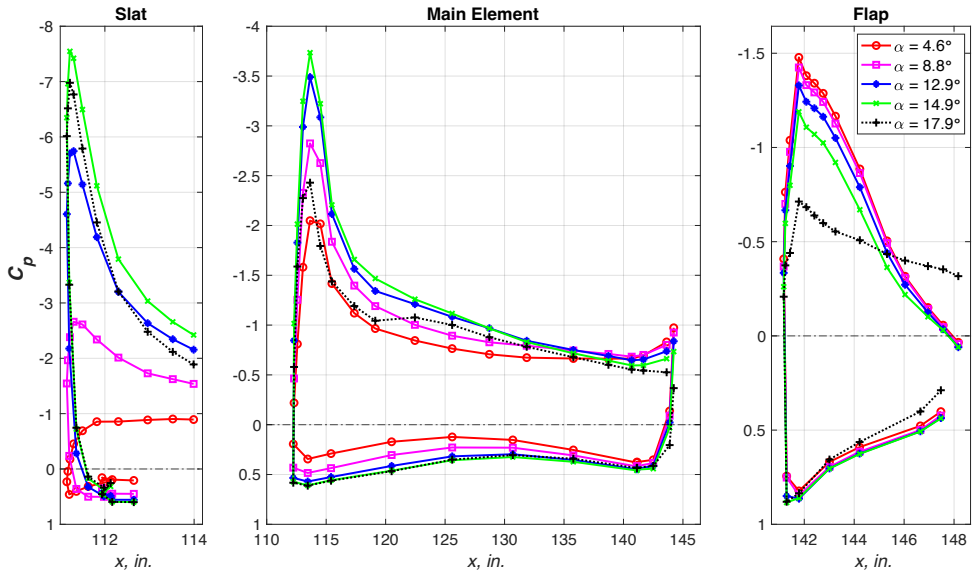

Fig. 17 C_p variation with α over the inboard section ($\eta = 24\%$, $\delta_a = 7.5°$).

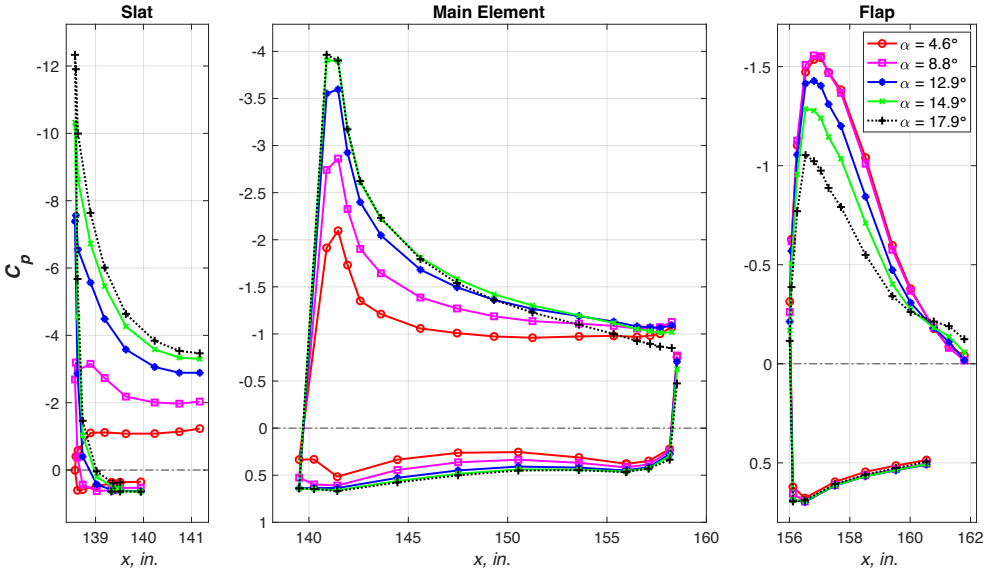

Fig. 18 C_p variation with α over the midboard section ($\eta = 55\%$, $\delta_a = 7.5°$).

The overall trend in the outboard C_p distributions (Fig. 19) is also similar to that of the nondeflected aileron case. One exception appears near the trailing edge of the aileron at $\alpha = 4.6°$. At this low angle of attack, the C_p distribution in Fig. 19a indicates a small flow separation bubble, which was attached flow for the nondeflected case. Flow separation moves upstream as we increase the angle of attack. We see higher suction pressures without pressure recovery over the aileron region due to flow separation. Similarly, for poststall (i.e., $\alpha = 17.9°$), flow over the main element is mostly separated starting from $x \sim 165$ in. at this spanwise location ($\eta = 82\%$). The same conclusions apply to the most outboard C_p distributions ($\eta = 91\%$, Fig. 19b). We see trailing-edge flow separation even at the lowest angle of attack ($\alpha = 4.6°$). As the angle of attack increases, we see higher suction peaks until stall, which dramatically decrease after stall. The trailing-edge flow separation moves upstream with increasing angle of attack and advances far upstream on the main element for $\alpha > 12.9°$. For post stall ($\alpha = 17.9°$), flow separation extends almost to the trailing edge of the slat and hence the flow over the entire main element appears separated.

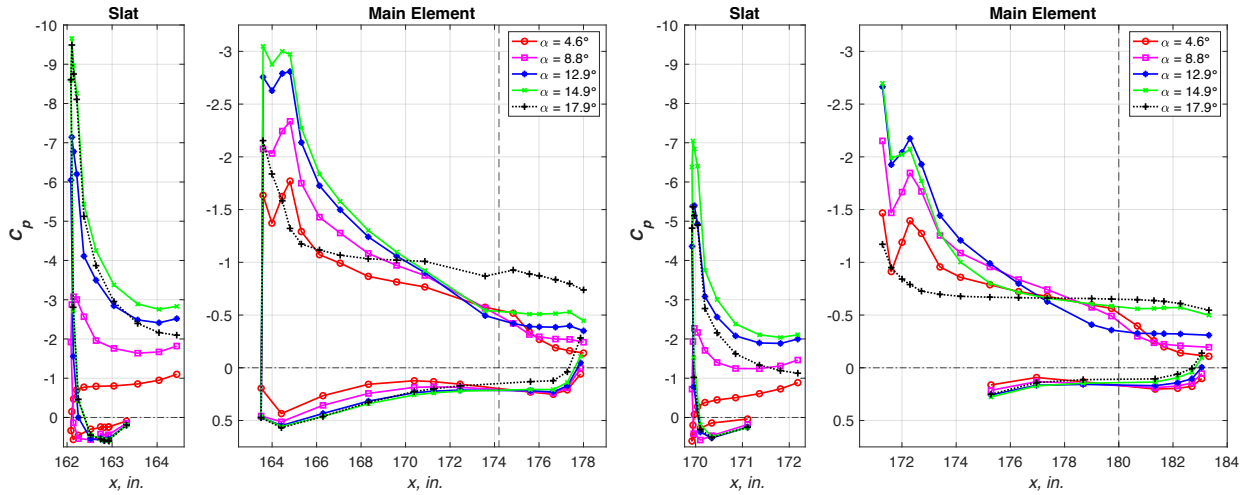

Fig. 19 C_p variation with α over the outboard sections (a) $\eta = 82\%$ (b) $\eta = 91\%$ ($\delta_a = 7.5°$).

Figure 20 compares the surface tuft flow visualization at different angles of attack when the aileron is deflected to the nominal deflection angle (δ_a = 7.5°). Surface minitufts indicate small trailing edge flow separation at α = 4.6°, which was attached for the nondeflected aileron case. Flow separation moves upstream with increasing angle of attack and extends to the entire aileron for α > 8.8°.

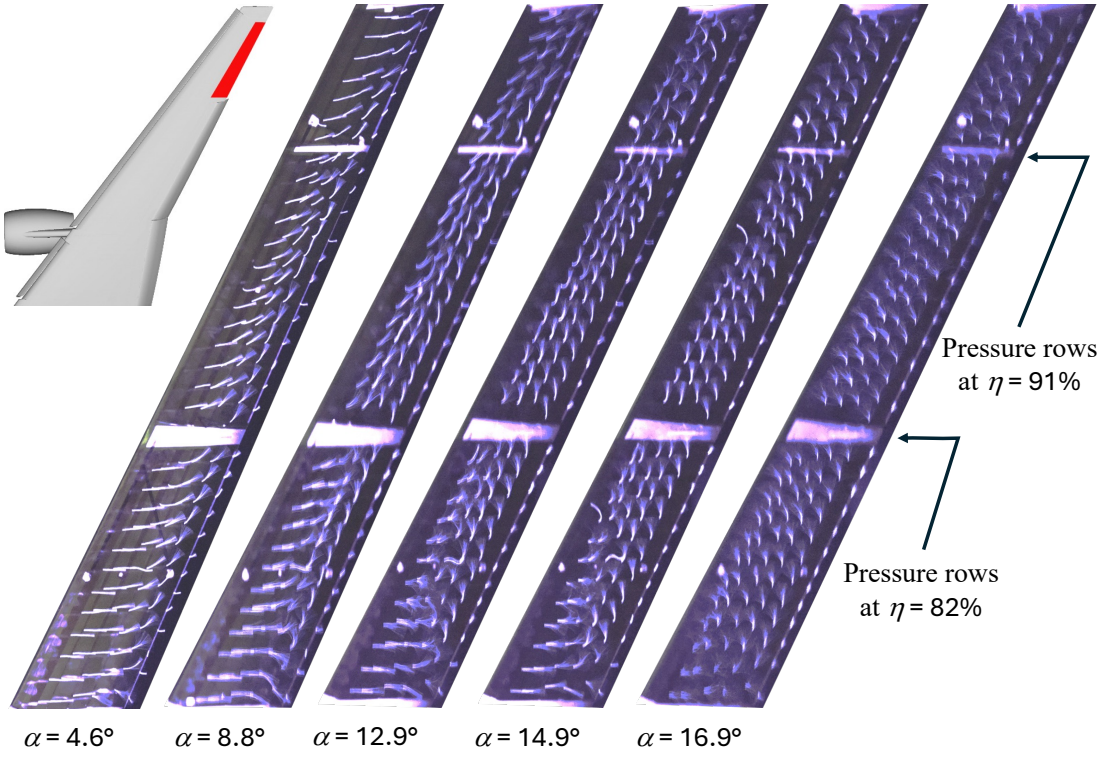

Fig. 20 Tuft flow visualization over the aileron ($\delta_a = 7.5°$).

C. High-Lift Improved Takeoff Configurations, $\delta_a = 16°$ and $\delta_a = 25°$

Leveraging the same principle, high-lift improved takeoff configurations can be achieved by deflecting the aileron more than the nominal deflection angle. In this study, we tested two aileron deflection angles of 16° and 25°. Fig. 21 shows the aerodynamic performance coefficients for different aileron deflections. As shown in Fig. 21a, the lift coefficient increases with the aileron deflection angle. The improvement is as much as ~0.06 at lower angles of attack and resulted in a C_{Lmax} of 2.137 at α_{max} = 15.5° for aileron deflection angle of 25°. An increase in the lift coefficient results in a more negative (nose down) pitching moment. As shown in Fig. 21c, the pitching moment decreases with the aileron deflection angle for the entire angle of attack range.

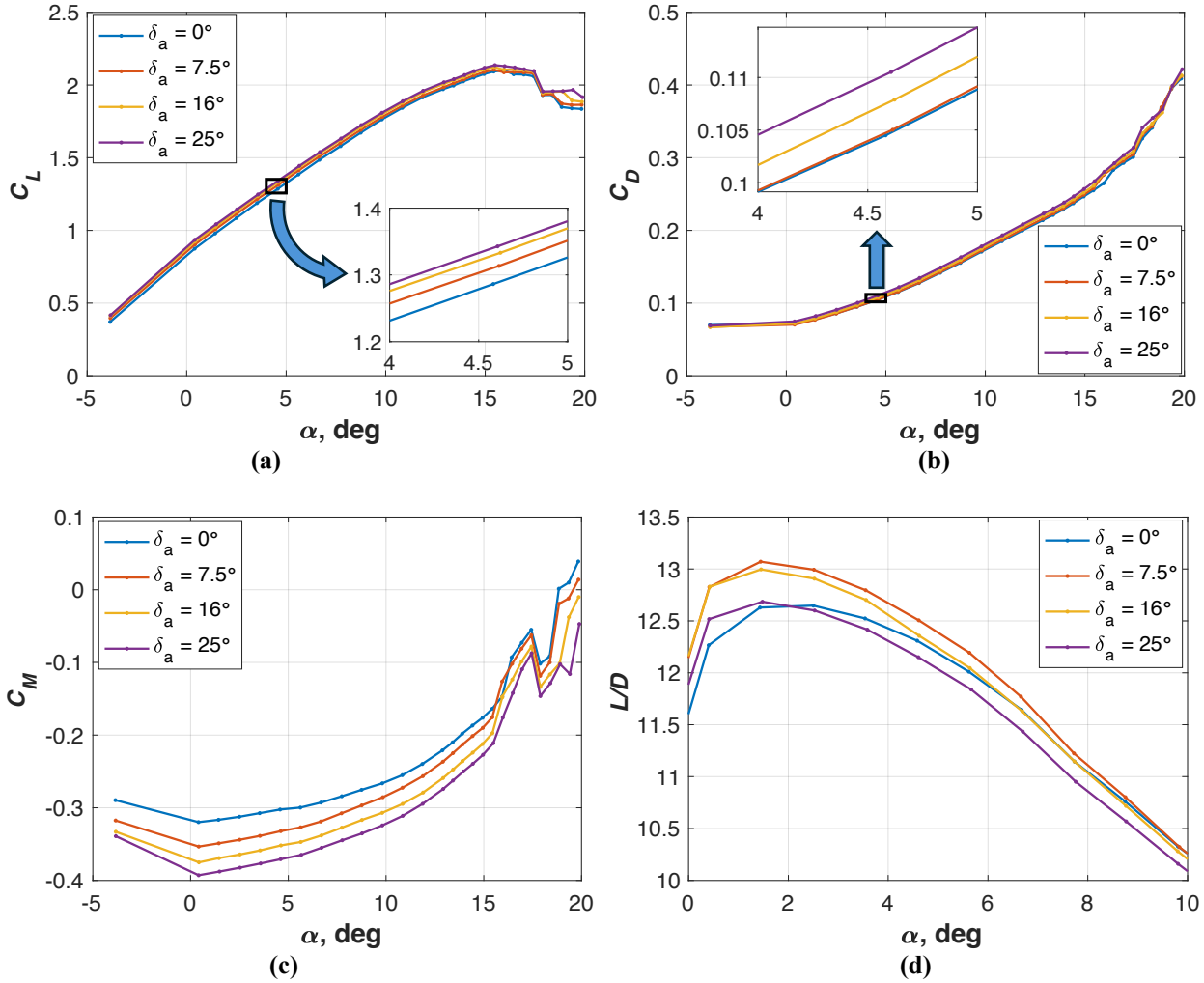

Fig. 21 Aerodynamic parameters for various aileron deflections at $\alpha = 4.6°$. (a) lift coefficient, (b) drag coefficient, (c) pitching moment coefficient, and (d) lift-to-drag ratio.

When the aileron is deflected more than the nominal deflection angle (δ_a = 7.5°), the flow over the aileron is separated even at lower angles of attack. The local flow separation over the aileron mainly affects the drag coefficient. Even though the drag coefficient was close for the $\delta_a = 0°$ and $\delta_a = 7.5°$ cases at $\alpha = 4.6°$, increasing δ_a to 16° and 25° results in drag increases of ~30 and ~55 counts, respectively (Fig. 21b). The increment in drag coefficient is consistent throughout the entire α range.

The combined effect of lift and drag increment with the aileron deflection angle is represented in the *L/D* plot (Fig. 21d). In this figure, the *x*-axis is zoomed into the $0° \le \alpha \le 10°$ range to highlight the differences. This plot also explains why the nominal aileron deflection angle was chosen as 7.5° as it provides the largest *L/D* for a takeoff angle of attack. Increasing the aileron deflection to 16° still resulted in a larger *L/D* compared to the nondeflected aileron

case, but a lower *L/D* compared to the nominal deflection angle. *L/D* improvement diminishes as the angle of attack increases despite the fact that the lift coefficient increases. This is due to the drag increase that is caused by the separated flow over the aileron. $\delta_a = 16°$ reaches similar *L/D* to the nondeflected case near $\alpha = 7°$. Even though the aileron deflection of 25° generated the largest improvement in the lift coefficient for a given α, the *L/D* performance is even worse than the nondeflected case, which is again due to the drag increase caused by the separated flow over the aileron.

Since the *L/D* performance reduction mainly comes from the drag increase due to flow separation, one can use AFC to control flow separation. Controlling flow separation not only reduces the drag but also increases lift and thereby improves the *L/D* performance further. Depending on the AFC blowing rate, up to 5-6 % improvement in *L/D* was shown both experimentally [18] and numerically [17]. The current wind tunnel results associated with flow control over the highly deflected aileron are presented in the companion paper [22].

Streamwise C_p distributions at the two outboard locations for different aileron deflections is presented in Fig. 22 for $\alpha = 4.6°$. As expected, the C_p distributions for the inboard and midboard sections are similar for different aileron deflections ($\delta_a = 16°$ and $\delta_a = 25°$), and therefore the results are not presented here. Increasing the aileron deflection improves the pressure distribution both on the suction and pressure surfaces for the entire chord at these two outboard locations. This is due to the increased circulation around the deflected aileron. The improvement in the C_p distribution is consistent with the increased lift coefficient that was observed for the larger aileron deflections in Fig. 21a. The pressure distribution over the aileron, which is denoted by the vertical dashed line in the plots, indicates attached flow for $\delta_a = 0°$ for the two outboard locations. When δ_a is increased to nominal aileron deflection ($\delta_a = 7.5°$), small trailing edge flow separation develops. The flow separation moves upstream (i.e., getting larger) as the aileron is deflected more. For $\delta_a = 25°$, flow over the entire aileron is separated even at this low angle of attack ($\alpha = 4.6°$).

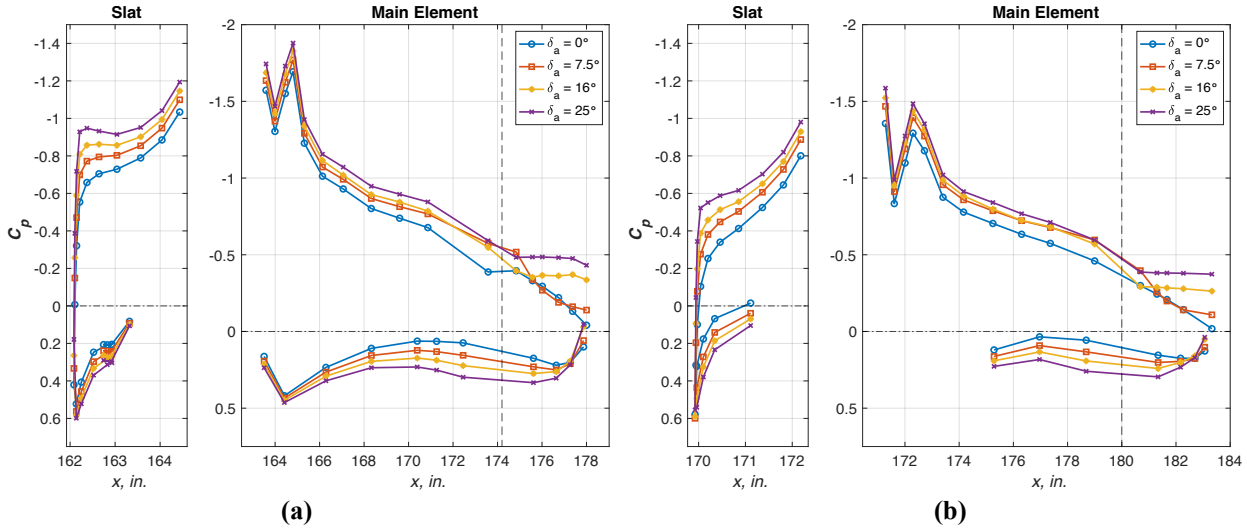

Fig. 22 C_p variation with δ_a over the outboard sections (a) $\eta = 82\%$ and (b) $\eta = 91\%$ ($\alpha = 4.6°$). Vertical dashed lines indicate aileron hinge location.

Surface tuft flow visualization presented in Fig. 23 confirms these conclusions. Again, attached flow is maintained at this angle of attack ($\alpha = 4.6°$) for the nondeflected aileron. At the nominal deflection angle ($\delta_a = 7.5°$), a small separation bubble develops at the trailing edge of the aileron (see last row of tufts near the trailing edge). Although we see spanwise flow both on the inboard ($\eta < 82\%$) and outboard ($\eta > 91\%$) side of the aileron, the tuft direction indicates attached flow at these regions. Thus, flow is mainly separated on the midsection of the aileron between these two pressure rows. Deflecting the aileron further to 16° and 25° results in separated flow for the entire aileron surface, which is consistent with the pressure distributions in Fig. 22.

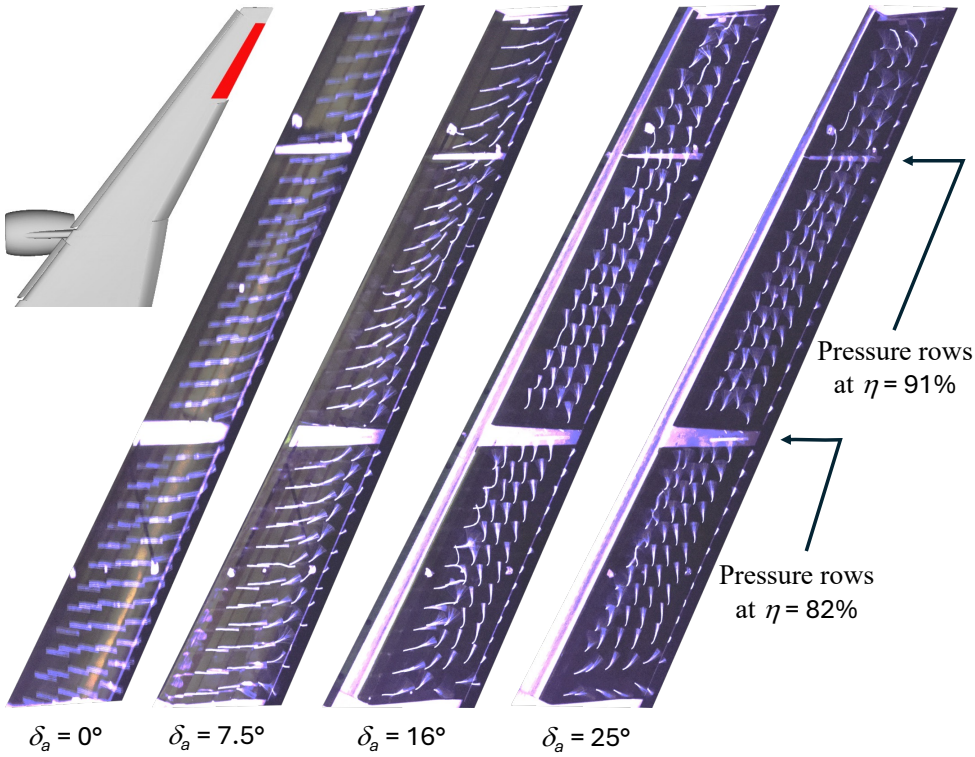

Fig. 23 Tuft flow visualization over the aileron for different aileron deflections at $\alpha = 4.6°$.

Variations in the C_p distribution over the outboard sections with angle of attack are presented in Fig. 24 for δ_a = 16°. The C_p distributions appear similar to those of the nominal aileron deflection case in Fig. 19 with the exception of the low angle of attack ($\alpha = 4.6°$) case. For the nominal deflection angle ($\delta_a = 7.5°$), the flow over the aileron was mostly attached where a small flow separation developed near the trailing edge of the midsection. However, for δ_a = 16°, the C_p distributions indicate separated flow over the aileron for all angles of attack. This observation is true for two outboard locations. Flow over the main element remains attached prior to stall for $\eta = 82\%$, whereas it separated earlier ($\alpha \leq 14.9°$) for the most outboard location ($\eta = 91\%$).

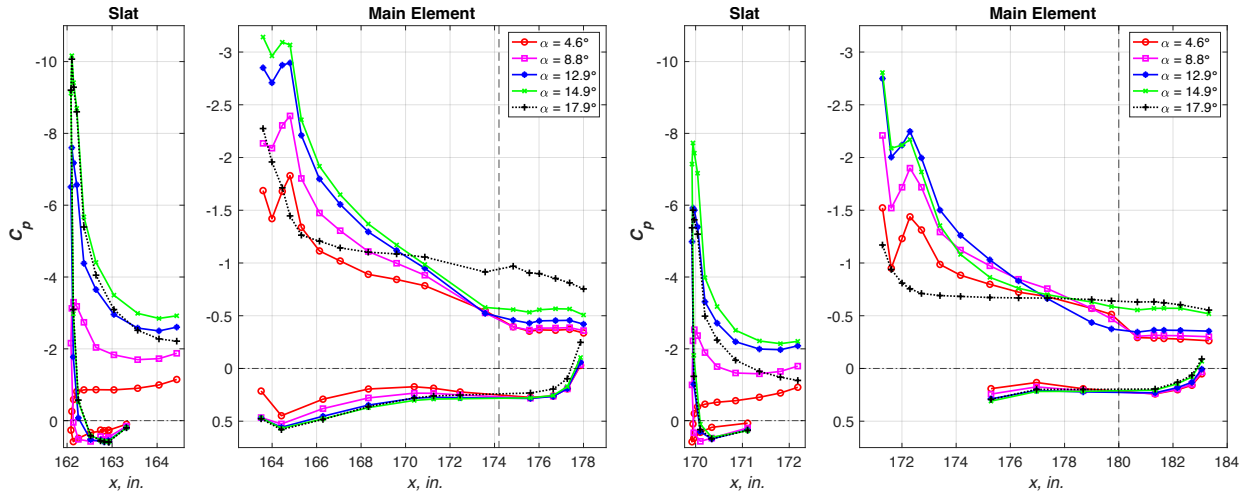

Fig. 24 C_p variation with α over the outboard sections (a) $\eta = 82\%$ and (b) $\eta = 91\%$ ($\delta_a = 16°$).

The C_p distributions over the outboard wing for $\delta_a = 25°$ are qualitatively similar to those of the $\delta_a = 16°$ case (Fig. 25). For this high aileron deflection, the flow over the aileron is separated even for low angles of attack. We see higher suction pressures over the main element and slat as the angle of attack increases until stall. The C_p distribution indicates flow separation over the main element for both outboard locations for post stall ($\alpha = 17.9°$). Similar to the other takeoff configurations, the most outboard location ($\eta = 91\%$) stalls at a lower angle of attack ($\alpha \leq 15°$) than that of the $\eta = 82\%$ location (Fig. 25b).

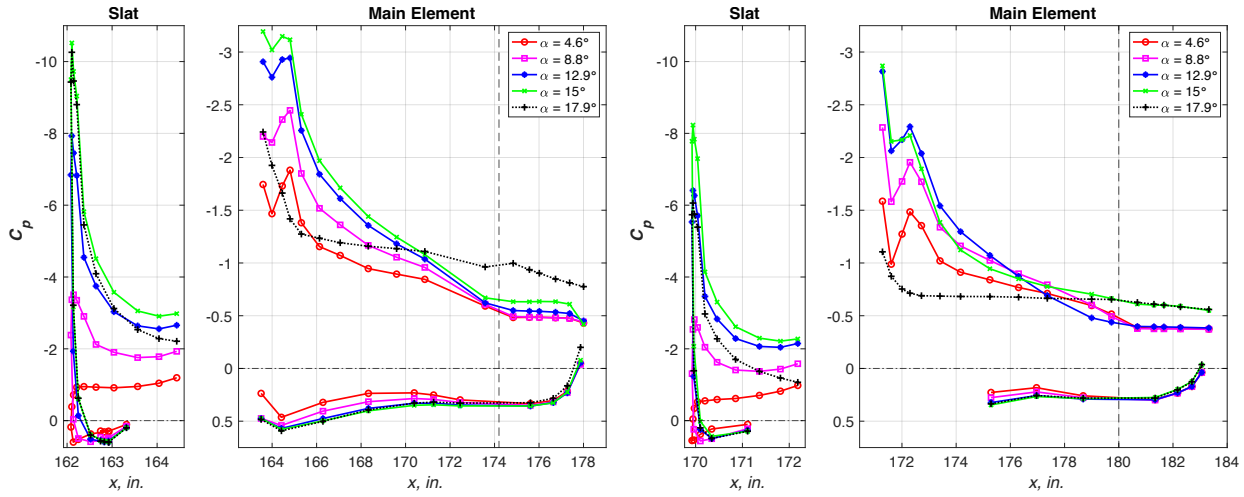

Fig. 25 C_p variation with α over the outboard sections (a) $\eta = 82\%$ and (b) $\eta = 91\%$ ($\delta_a = 25°$).

Limited tuft flow visualization was performed to see the flow behavior over the aileron and the main element (Fig. 26). In this configuration, the aileron was deflected to 16° and Mach number was 0.26. Note that these are uncorrected angles of attack (α_u) values. Although there was a subtle difference in the slat rigging, this difference would not change the qualitative observations. At lower angles of attack ($\alpha_u < 12°$), separated flow is observed over the entire aileron whereas flow is attached on the main element. Increasing the angle of attack to $\alpha_u = 12°$ resulted in a more adverse pressure gradient. Flow separation moves slightly upstream to the trailing edge of the main element over the outboard section of the aileron. When the angle of attack is further increased to $\alpha_u = 14°$, flow separation not only moves upstream but also progresses inboard. Flow separation reaches almost to the slat trailing edge near the wing tip and to the trailing edge of the main element near $\eta = 82\%$ spanwise location. For $\alpha_u = 15°$, flow separation progresses more inboard, and we see separated flow for most of the main element.

The C_p distributions over the outboard wing are presented in Fig. 27 for the same angles of attack to compare with the tuft flow visualization. In order to capture the stall progress behavior, the C_p distributions at $\eta = 82\%$ and $\eta = 91\%$ spanwise locations are provided only over the main element with aileron (i.e., the slat is omitted). Similar to the flow visualization figure, these are uncorrected angles of attack. The C_p distributions indicate separated flow over the aileron for all angles of attack at both spanwise locations consistent with the flow visualization. The attached flow is maintained over the main element for $\alpha_u = 10°$ and 12°. When the angle of attack is increased to $\alpha_u = 14°$, the C_p distribution at $\eta = 82\%$ location still indicates attached flow over the main element; however, it is separated for $\eta = 91\%$ location as indicated by the plateau in the C_p distribution (x ~ 173 in). These observations are in line with Fig. 26 where flow separation advanced upstream to the main element for $\alpha_u = 14°$ at $\eta = 91\%$, but attached flow was observed over the main element for $\eta = 82\%$ location. When the angle of attack is increased to 15°, the C_p distributions indicate separated flow for both locations, again consistent with the flow visualization showing that the stall progressed inboard.

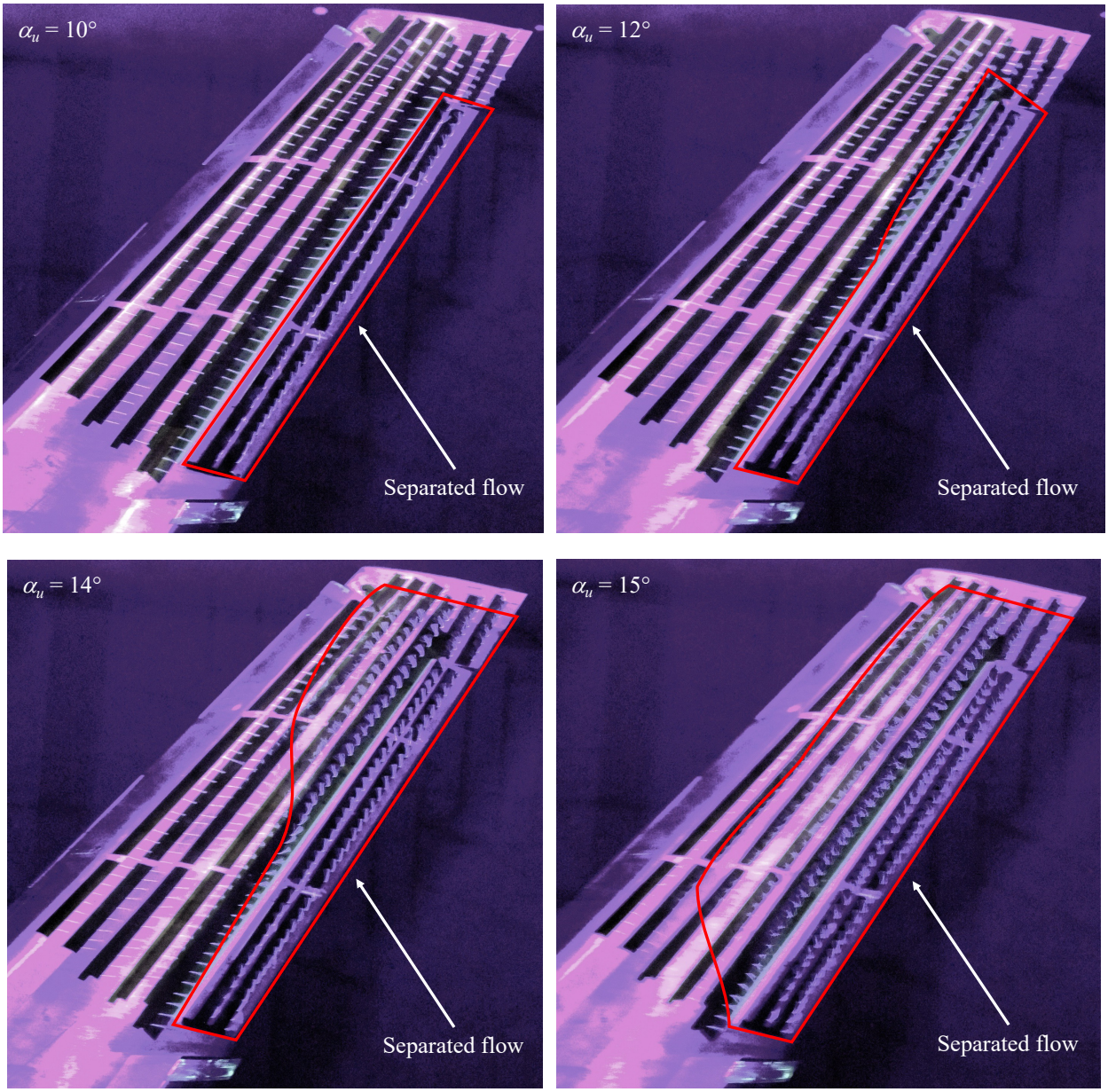

Fig. 26 Tuft flow visualization over the outboard wing showing the stall progression (δ_a = 16°, M = 0.26).

If we compare the takeoff flow visualization in Fig. 26 to the previously reported landing flow visualization [28], we notice a different stall progression over the outboard wing. It was reported both numerically and experimentally [28] that the outboard wing exhibits pockets of local flow separation regions (sometimes referred to as "pizza slice" shaped flow separation patterns) downstream of the slat brackets near the trailing edge (Fig. 28). These pockets of local flow separation are caused by the interaction of the slat bracket wakes with the adverse pressure gradient and gradually increase in size as the angle of attack increases. Except for the local flow separation, attached flow is maintained over most of the outboard wing even after stall (α_u > 16°) for the landing configuration [28]. This is possibly due to the slotted slat which helps the boundary layer to withstand the adverse pressure gradient. As a result, the outboard wing stalls after the inboard wing for the landing configuration. However, for the takeoff configurations with sealed slat, it is shown in the current study that the stall is initiated over the most outboard wing first. As the angle of attack increases, stall gradually moves upstream, reaching the slat trailing edge and also progressing inboard. Even at α_u = 15°, the flow over the entire outboard wing is separated.

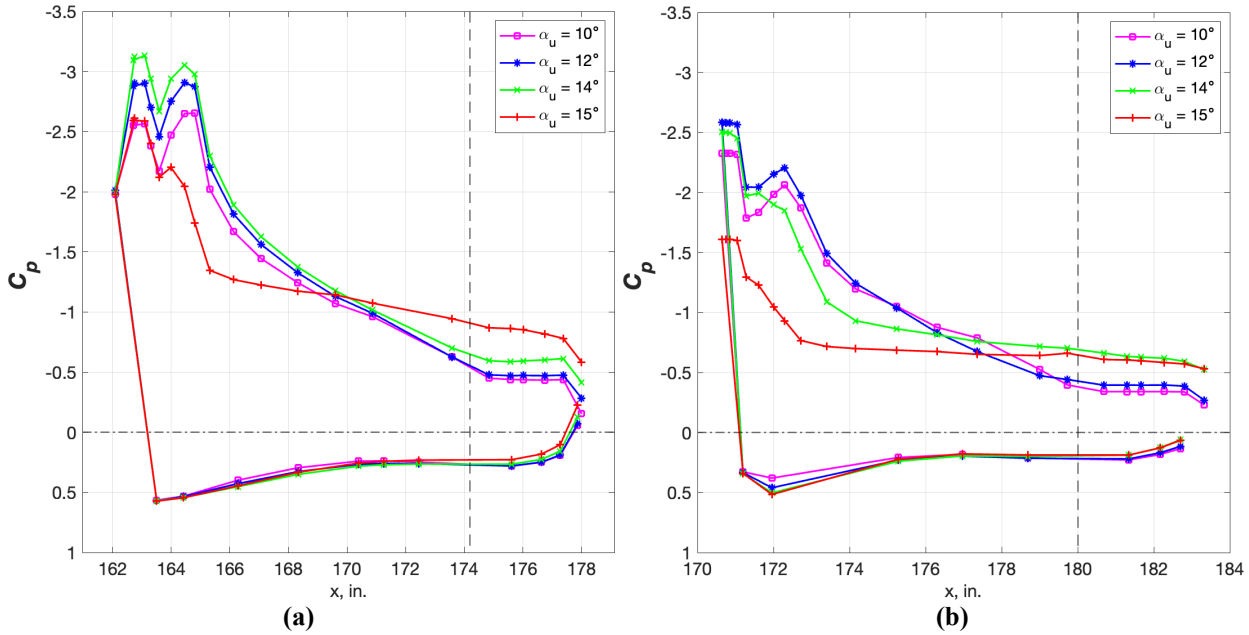

Fig. 27 C_p variation with α_u on the main element at two outboard locations (a) $\eta = 82\%$ and (b) $\eta = 91\%$ ($M = 0.26$, $\delta_a = 16°$).

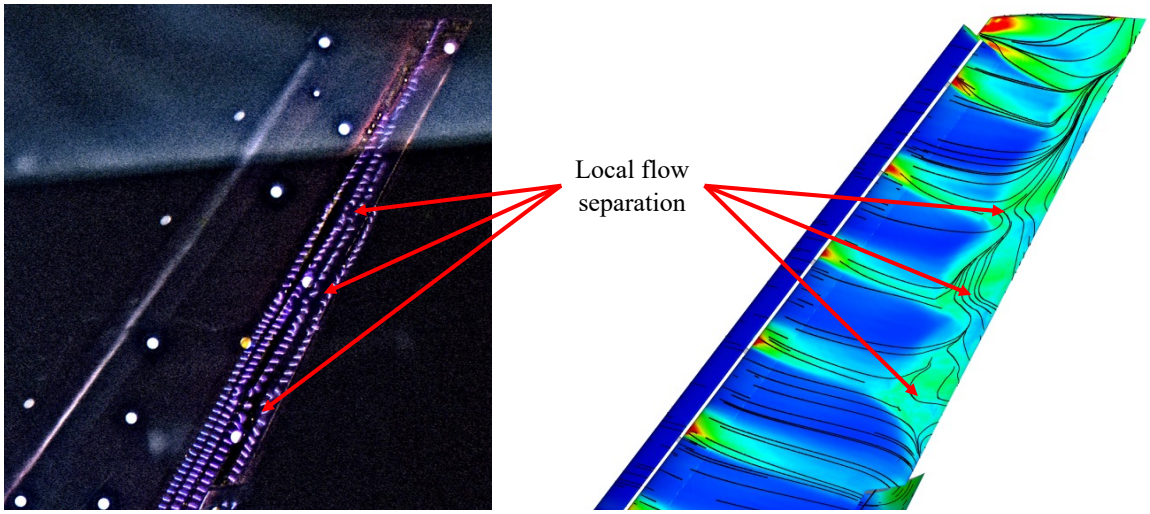

Fig. 28 Flow separation over the outboard wing for the landing configuration ($M = 0.2$, $\delta_a = 0°$, $\alpha_u = 16°$) [28].

IV. Summary and Conclusion

The 10% scale High-Lift Common Research Model (CRM-HL) was tested in the NASA Langley 14- by 22-Foot Subsonic Tunnel (14x22) in support of the of NASA Advanced Air Transport Technology (AATT) Project. The main objective of the wind tunnel tests was to improve the aerodynamic performance during takeoff operations using localized active flow control (AFC). The assessment of AFC configurations and high-lift improvement results are reported in a companion paper. The focus of the current paper is to report the data relevant to the CRM-HL takeoff configurations and establish a reference case for localized AFC applications. Wind tunnel measurements included surface static pressures, force and moment data, and limited minituft flow visualization. Data is corrected for wind tunnel wall interference. Although the effect of Reynolds numbers is investigated, most of the measurements are reported for the freestream Mach number (M) of 0.2.

Three different takeoff—reference, nominal, and high-lift improved—configurations are documented. These takeoff configurations are obtained by varying aileron deflection. The reference takeoff configuration is the takeoff configuration defined by the CRM-HL ecosystem. This takeoff configuration includes 25° flaps, 22° slats with sealed slat gap, and nondeflected aileron. The stall angle of attack (α_{max}) for the reference takeoff configuration is found to be as α_{max} = 15.9° with a maximum lift coefficient (C_{Lmax}) of 2.1 at M = 0.2. The nominal takeoff configuration is similar to the reference takeoff configuration, except the aileron deflection angle (δ_a) is 7.5°. The aileron deflection slightly increases the maximum lift coefficient (C_{Lmax} = 2.105 at α_{max} = 15.4°) at the expense of a very small trailing edge flow separation. Consequently, the nominal takeoff configuration results in a maximum increase in the lift-to-drag (L/D) ratio of 4% compared to the reference takeoff configuration.

The high-lift improved takeoff configurations are based on the same principle, whereby the aileron is deflected further to improve the takeoff high-lift aerodynamics. However, these cases are intended to be used together with a flow control strategy to reduce the flow separation that develops at higher aileron deflections. Two different aileron deflections are tested in this wind tunnel campaign (δ_a = 16° and δ_a = 25°). Increasing the aileron deflection increases the lift coefficient (C_{Lmax} = 2.125 and C_{Lmax} = 2.137, respectively); however, the drag increases as well. The combined effect (L/D) shows reduced aerodynamic performance compared to the nominal takeoff configuration when flow control is not used. Since the lift coefficient increases with aileron deflection, the high-lift performance decrease comes from the drag increase due to flow separation. Once a flow control strategy is applied to reduce or eliminate the flow separation, one can increase the high-lift performance (i.e., L/D) as much as 5% using onboard resources as compared to the nominal takeoff configuration. The results presented in this study could be used in the CRM-HL ecosystem as well as any future high-lift research for localized or different AFC applications.

Acknowledgments

This research was funded by the Airframe Technologies Subproject of the Advanced Air Transport Technology Project in the NASA Advanced Air Vehicles Program. The authors are extremely grateful to the staff of the 14x22 for their support and the efforts taken to ensure the data quality met the test requirements. The authors also thank model designer Sandy Webb (design of the AFC aileron for the 10% scale model), Danny Lovaglio and Tom Hall (static and dynamic pressure instrumentation), Rob Andrews (SLA actuator fabrication), and the NASA Langley machine shop (pre-test hardware modifications and repairs).

References

[1] Van Dam, C. P., "The Aerodynamic Design of Multi-Element High-Lift Systems for Transport Airplanes," *Progress in Aerospace Sciences*, Vol. 38, 2002, pp. 101–144.

[2] Lin, J. C. and Dominik, C. J., "Parametric Investigation of a High-Lift Airfoils at High Reynolds Numbers," *Journal of Aircraft,* Vol. 34, No. 4, July–August 1997, pp. 485-491.

[3] Gatlin, G. M. and McGhee, R. J., "Experimental Investigation of Semispan Model Testing Techniques," *Journal of Aircraft*, Vol. 34, No. 4, July–August 1997, pp. 500-505.

[4] Storms, B. L., James, K. D., Satran, D. R., Arledge, T., K., Burnside, N, J., Horne, W. C., and Driver, D. M., "Aerodynamics of a 26%-Scale Semi-Span Model of the Boeing 777 in the NASA Ames 40- by 80-Foot Wind Tunnel," NASA/TP–2005-212829, January 2005.

[5] Hannon, J. A., Washburn, A. W., Jenkins, L. N., and Watson, R. D., "Trapezoidal Wing Experimental Repeatability and Velocity Profiles in the 14- by 22-Foot Subsonic Tunnel," AIAA Paper 2012-0706, January 2012.

[6] Lacy, D. S. and Sclafani, A. J., "Development of the High Lift Common Research Model (HL-CRM): A Representative High Lift Configuration for Transonic Transports," AIAA Paper 2016-0308, January 2016.

[7] Clark, A. M., Slotnick, J. P., Taylor, N. J., and Rumsey, C. L., "Requirements and Challenges for CFD Validation Within the High-Lift Common Research Model Ecosystem," AIAA Paper 2020-2772, June 2020.

[8] Lin, J. C., Melton, L. P., Hannon, J. A., Andino, M. Y., Koklu, M., Paschal, K. B., and Vatsa, V. N., "Testing of High-Lift Common Research Model with Integrated Active Flow Control," *Journal of Aircraft*, Vol. 57, No. 6, 2020, pp. 1121–1133.

[9] Lin, J. C., Melton, L. P., Hannon, J., Koklu, M., and Andino, M., "Semispan Test Results of a Conventional High-Lift Common Research Model in Landing Configuration," NASA TP 20220008270, August 2022.

[10] D. P. Lockard, T. L. Turner, C. J. Bahr and F. V. Hutcheson, "Overview of Aeroacoustic Testing of the High-Lift Common Research Model," AIAA paper 2021-2113, August 2021.

[11] Evans, A. N., Lacy, D. S., Smith, I., and Rivers, M. B., "Test Summary of the NASA High-Lift Common Research Model Half-Span at QinetiQ 5-Metre Pressurized Low-Speed Wind Tunnel," AIAA Paper 2020-2770, June 2020.

[12] Lacy, D. and Clark, A. M., "Definition of Initial Landing and Takeoff Reference Configurations for the High Lift Common Research Model," AIAA paper 2020-2771, June 2020.
[13] Rumsey, Ch. L., Slotnick, J. P., and Sclafani, A. J., "Overview and Summary of the Third AIAA High Lift Prediction Workshop," AIAA Paper 2018-1258, January 2018.
[14] Rumsey, Ch. L., Slotnick, J. P., and Woeber, C. D., "HLPW-4/GMGW-3: Overview and Workshop Summary," AIAA Paper 2022-3295, June 2022.
[15] Lin, J. C., Melton, L. P., Hannon, J. A., Andino, M. Y., Koklu, M., Paschal, K. B., and Vatsa, V. N., "Semispan Test Results of an Active Flow Control Enabled High-Lift Common Research Model in Landing Configuration," NASA TP 20220015673, December 2022.
[16] Woszidlo, R., Shmilovich, A., and Vijgen, P., "Low-Speed Performance Enhancement using Localized Active Flow Control – Program Overview and Summary", NASA CR 20220006728, April 2022.
[17] Shmilovich, A., Yadlin, Y., Vijgen, P. M., and Woszidlo, R., "Flow Control for Enhanced Aileron Effectiveness on a Commercial Aircraft," AIAA Paper 2023-0655, January 2023.
[18] Melton, L. P., Koklu, M., Andino, M. Y., and Hannon, J. A., "Wind Tunnel Testing of AFC over a Deflected Aileron on the High-Lift Common Research Model," AIAA Paper 2024-3672, July 29 – August 2, 2024.
[19] Garner, P., Meredith, P., and Stoner, R., "Areas for Future CFD Development as Illustrated by Transport Aircraft Applications," AIAA Paper 1991–1527, June 1991.
[20] Shmilovich, A., Vijgen, P., and Woszidlo, R., "Low-Speed Performance Enhancement using Localized Active Flow Control – Localized Active Flow Control Simulations on a Reference Aircraft", NASA CR 20220006731, April 2022.
[21] Vijgen, P., Ziebart, A., Shmilovich, A., and Woszidlo, R., "Conceptual Integration Studies of Localized Active Flow Control on the Wing of a Commercial Aircraft," AIAA Paper 2023-0657, January 2023
[22] Andino, M. Y., Melton, L. P., Koklu, M., and Hannon, J. A., "Active Flow Control Enhanced Aileron of the High-Lift Common Research Model at Takeoff Condition," AIAA Paper 2025-xxxx, January 2025.
[23] Gentry, G. L., Jr., Quinto, P. F., Gatlin, G. M., and Applin, Z. T., "The Langley 14- by 22-Foot Subsonic Tunnel: Description, Flow Characteristics and Guide for Users," NASA TP 3008, September 1990.
[24] Neuhart, D. H., and McGinley, C. B., "Free-Stream Turbulence Intensity in the Langley 14- by 22-Foot Subsonic Tunnel," NASA TP 2004-213247, August 2004.
[25] Iyer, V., Kuhl, D. D., and Walker, E. L., "Improvements to Wall Corrections at the NASA Langley 14X22-Foot Subsonic Tunnel," AIAA Paper 2003-3950, June 2003.
[26] Shmilovich, A., Stauffer, M., Woszidlo, R., and Vijgen, P., "Low-Speed Performance Enhancement using Localized Active Flow Control: Simulations, Scaling and Design of Localized Active Flow Control on the Common Research Model (4/4)," NASA CR 20220006736, April 2022.
[27] Pülm, S., Schmidt, F., Rudnik, R., and Winski, C., "Low-Speed Testing of the 5.2% Semispan CRM-HL in the DNW-NWB Wind Tunnel," AIAA Paper 2024-3516, July 29 – August 2, 2024
[28] Koklu, M., Lin, J. C., Hannon, J. A., Melton, L. P., Andino, M. Y., Paschal, K. B., and Vatsa, V. N., "Investigation of the Nacelle/Pylon Vortex System on the High-Lift Common Research Model," *AIAA Journal*, Vol. 59, No. 9, 2021, pp. 3748–3763.